MODELING OF SEISMOELECTRIC EFFECTS IN A BOREHOLE

Matthijs W. Haartsen and M. N. Toksöz

Earth Resources Laboratory
Department of Earth, Atmospheric, and Planetary Sciences
Massachusetts Institute of Technology
Cambridge, MA 02139

ABSTRACT

We present a method to simulate the propagation of seismic and converted electromagnetic waves generated by a mechanical borehole source embedded in a layered poroelastic medium. The electroseismic conversions occur at both the borehole wall and the layer boundaries. Most studies in electroseismic effects have been modelled and tested with seismic sources and detectors (geophones and antennas) at the surface. In this paper, we investigate the case of a seismic source in a borehole and receivers either at the surface or embedded in the medium. The method is formulated as a boundary element technique (where the poroelastic displacement and relative flow Green's functions are calculated by the discrete wavenumber method. The singular properties of the Green's functions are determined analytically using static Green's functions to regularize the integrals. This is necessary to calculate the element's self interaction. The borehole is cylindrical and its axis runs normal to the interfaces. The coupled electroseismic effects in the layered media are included by using the global matrix technique.

The developed method is an extension of the model of Biot-Rosenbaum, who applied the wavenumber integration technique to investigate the effect of formation permeability on Stoneley waves, using Biot's theory to model the wave propagation effects of a homogeneous permeable formation surrounding a borehole. We extend the Biot-Rosenbaum model by including the effect of a heterogeneous permeable formation surrounding the borehole. The effect of formation permeable zones (or fractured zones) on Stoneley waves can now be investigated. The other modification is the inclusion of conversions of mechanical into electromagnetic waves at mechanical and/or electrical contrasts in the poroelastic formation. The converted electromagnetic fields are sensitive to large permeability contrasts and fluid chemistry contrasts inside a reservoir. Using the electroseismic method downhole will provide more information about permeability/permeability

contrasts in the formation, as well as additional lithological information (salinity of the fluids).

INTRODUCTION

Many rocks in the upper crust have porosity and are characterized as porous, permeable media. The determination of fluid-flow properties as well as fluid properties of sedimentary rocks is of great importance in groundwater hydrology studies, in environmental problems, and in the evaluation of hydraulic conductivity and fluid contrasts inside reservoirs in the petroleum industry. Full waveform acoustic logging offers an effective tool for characterizing permeable sand-shale sequences found in sedimentary formations. The stratigraphic permeable traps are important in the exploration and production of hydrocarbons.

The theoretical foundations of the study of acoustic wave propagation in a cylindrical borehole was laid by Biot (Bouchon, 1952), who presented a derivation of the period equation for borehole guided waves and their dispersion characteristics. The current technique to model borehole acoustic wave propagation through heterogeneous formation is the finite difference method (Cheng, 1994; Stephen and Cheng, 1985). The numerical difficulty of using explicit time marching FD, to model wave phenomena through porous media is caused by the dispersive nature of Biot's slow wave (Biot, 1956) and the coupling of this wave with fast and shear waves. The wavenumber intergration technique has been applied to calculate wave propagation in homogeneous porous formations. Rosenbaum (1974) investigated the effect of formation permeability using Biot's theory at high frequencies, combined with the open pore boundary conditions proposed by Deresiewicz and Skalak (1963) to model wave propagation effects of a homogeneous permeable formation surrounding a borehole. Schmitt and Bonnet (1988) investigated the case of a borehole surrounded by multiple radially layered isotropic poroelastic layers and modified later his theory to the more complicated case of a borehole surrounded by a radially transversely isotropic layered poroelastic medium (Schmitt, 1989).

In this paper, we generalize the Biot-Rosenbaum model with two modifications. We apply a BEM modelling technique to simulate wave propagation inside the borehole and outside the borehole in a heterogeneous poroelastic formation. At the mechanical and/or electrical boundaries in the formation, the conversions from mechanical into electromagnetical waves are included. Before we outline the method to simulate the propagation of seismic and converted electromagnetic waves generated by a mechanical borehole source embedded in a layered poroelastic medium, we want to discuss the importance of measuring the acoustic fields and electromagnetic fields inside the borehole with respect to their dependence on permeability and fluid chemistry.

The fundamental mode of a guided wave travelling in a fluid column, the Stoneley wave, is an interface wave and it is therefore sensitive to formation properties, such as density, moduli and, most importantly, permeability. Field experiments clearly indicate the effect of formation permeability on borehole Stoneley waves (Williams *et al.* (1984).

Seismoelectric Effects in a Borehole

Theoretical models were developed to study the correlation between permeability and Stoneley wave propagation. White (1983) and Hsui and Toksöz, (1986) developed low frequency models of Stoneley wave propagation. Rosenbaum (1974) investigated the effects of permeability on high frequency borehole acoustic waves. Burns and Cheng (1986) went a step further and inverted for in-situ permeability from Stoneley wave velocity and attenuation using the Biot-Rosenbaum model. Winkler and Johnson (1989) performed laboratory model experiments on borehole Stoneley wave propagation to evaluate the applicability of the Biot theory to logging in porous formations. The theory was found to be in agreement with the experiments.

Others have tried to obtain fracture information from Stoneley wave measurements. Hornby and Plumb (1989) and Tang (1990) model both attenuation and reflection of Stoneley waves from a single plane fracture. They conclude that it takes a rather large fracture aperture of the order of centimeters, to get a significant Stoneley wave attenuation. Paillet and Tang (1989) suggest that in-situ fractures may consist of an array of flow passages or fracture layers instead of a single fluid layer. This suggests modeling fractures as a permeable zone in the formation. Key parameters used to characterize the permeable zone are thickness of the zone, permeability, porosity, and tortuosity. Since the last three parameters typically describe a porous model, we can use the Biot-Rosenbaum theory (Tang and Cheng, 1993) to model Stoneley wave characteristics in the permeable zone. Tang and Toksöz (1991) developed a simplified model for Stoneley wave propagation in a permeable formation, which is consistent with the Biot-Rosenbaum theory in the presence of a hard formation.

The approach we present in this chapter relies on the important conclusion that fractured zones can be characterized using Biot's theory. The model has no real frequency constraints, as long as we are in the seismic/acoustic logging regime, and is applicable to heterogeneous porous formations. Winkler and Johnson (1989) predict in their theoretical calculations that in a $k = 10^{-14}m^2$ rock, the effect of permeability is to decrease the Stoneley velocity by less than 1 percent which is less than the uncertainty in Stoneley velocity measurements. Therefore they conclude that a $k = 10^{-14}m^2$ permeabiliy is probably a lower limit to what can be expected to measure in the field using Stoneley velocities.

Additional information about very low permeability zones might be obtained, however, using the converted electric fields at high permeability contrasts. The amplitude of a converted electromagnetic field is sensitive to large permeability contrasts of the permeable sand impermeable shale type. The permeabiliy of the formation can play an important role in the determination of the formation's electrical conductivity. The electrical conductivity increases monotonically with increasing porosity since the amount of bulk electrolyte increases linearly with porosity, (see Haartsen, 1995, chapter 2). This increase in conductivity is not linear with porosity due to the porosity dependence of the pore length parameter, which influences the conductivity enhancement due to surface conductances. The electrical conductivity decreases with increasing permeability. At very small permeabilities the surface conductances become important and dominate in

value the conductivity contribution of the bulk conductivity in the fluid phase, (Haartsen, 1995, chapter 2). Physically this situation occurs when the pore space is filled with clay, reducing the permeability of the formation but not affecting the porosity, this greatly enhancing the conductances along the pore surfaces (Haartsen, 1995, chapter 2). When mechanical waves traverse such a permeability contrast, the induced electric fields at both sides of the interface experience a different electrical conductivity and produce a dynamic current imbalance which causes electromagnetic radiation.

Electroseismic conversions are also sensitive to fluid chemistry contrasts inside a homogeneous reservoir. The Stoneley waves in the borehole won't be affected by the different fluids, provided that the densities and viscosities of the two fluids are approximately the same. The body waves in the surrounding poroelastic formation are also not affected since the different saturating fluids cause only a negligible mechanical contrast.

STRATEGY TO SIMULATE COUPLED ACOUSTO-ELASTIC AND ELECTROMAGNETIC WAVES IN BOREHOLE GEOMETRY

The boundary element modelling technique (see Brebia and Dominguez, 1989, for general discussion on different types of BEM) is formulated to solve a vertical waveguide (borehole) which penetrates a horizontal flat layered poroelastic medium. We follow closely the boundary element based modelling technique proposed by Bouchon (1993). Bouchon used the method to solve the wavefield problem in an infinite open borehole and in the surrounding isotropic layered elestic formation. Dong (1993) added two extensions to Bouchon's modelling technique; he generalized the formation to include transversely isotropic layers and included casing in his formulation.

In our formulation at the layer boundaries, mechanical waves are partly converted into electromagnetic fields, satisfying all mechanical and electromagnetical boundary conditions. The conversion to electromagnetic fields induced by the mechanical tube waves is also included. But these electromagnetic fields don't satisfy the EM boundary conditions on the borehole wall. We first describe the BEM implementation. Since four boundary conditions have to be complied with at the borehole wall, four fictitious ring sources need to be introduced. The P wave radiation in the borehole is uniquely described by a fluid volume injection ring source. The $P_f - SV - P_s$ wave radiation in the poroelastic formation are determined by the vertical, radial ring sources applied to the frame and by an explosive ring source on the fluid phase, respectively. The field vector components for each ring source are obtained by integrating the appropriate Green's functions directly over a ring. The poroelastic Green's functions are given in the appendix and derived in (Haartsen, 1995, chapter 5). The final fields are obtained by surface integrating the dynamic Green's functions. The integrals are first reduced to horizontal wavenumber integrals and solved by discrete wavenumber summation. BEM modelling requires the calculation of a square boundary condition matrix containing the wavenumber interaction results between all elements. To calculate the elements' self interaction, the singular properties of the Green's functions need to be determined.

The stress field for the dynamic Green's functions with a force on the solid phase is singular, and the displacement for the dynamic Green's functions with a force on the fluid is also singular. The contribution of the stress and displacement singularities, when source and receiver coincide, are determined analytically by integration of the static Green's functions over a half spherical surface.

The last part of this paper discusses the inclusion of horizontal layers coupled to the borehole using the BEM modelling technique. At the horizontal interfaces, the electroseismic governing equations (Haartsen, 1995, chapter 2) with boundary conditions added are solved numerically. Biot's equations with an induced body force on Biot's equation of relative flow, and Maxwell's equations with an induced current source, and all the mechanical to electromagnetic coupling present in the transport equations, are solved simultaneously. A mechanical poroelastic displacement/stress and coupled electromagnetic wavefield component vector as a function of depth can be determined, which equals the so called system matrix, containing all medium properties and electrokinetic and osmotic coupling, times the same displacement/stress/EM wavefield component vector. The eigenvalues (slownesses) and corresponding up and down going fast, slow, SV and TM polarized wavefield eigenvectors of the coupled electromagnetic and acoustic-elastic system matrix are derived in Haartsen (1985, chapters 3 and 4).

To solve simultaneously the macroscopic electromagnetic and acoustic-elastic wavefields in layered media we use the global matrix method. We derive source jump representations for the introduced ring sources using the relative flow and displacement Green's functions together with the deformation equations in both phases. These mechanical sources generate fluid flow and electrical streaming current in the porous medium. Both current and fluid flow are related through the transport equations through which all electro-mechanical coupling occurs. At the borehole wall the mechanical waves are matched only. The effect of the borehole on the electromagnetic fields is assumed to be insignificant since the electromagnetic wavelengths are for typical circumstances (100 Hz seismic center frequency in the numerical modelling) on the order of a kilometer, while the borehole radius has typically a diameter of 20 cm.

In this paper, we will discuss the numerical results of the newly derived vertical, radial and volume injection ring sources in layered porous media. These calculation routines constitute the kernel of the BEM algorithm. The sum of the weighted ring sources determines the wavefields radiated into the formation. The weighting of each source is determined by solving a linear system of equations that incorporate the mechanical boundary conditions on the borehole wall. The calculation of all element interactions for all wavenumbers for all frequencies is numerically feasible on a massive parallel computer (the BEM algorithm was implemented on ERL's nCUBE), but its long run time does not allow practical wave propagation study. Therefore, we have chosen to present the numerical comparison of the three ring sources in poroelastic layered media. The electromagnetic radiation induced by the mechanical vertical and radial ring sources is discussed. The conversion to electromagnetic disturbances generated by P and SV waves is studied for the three different ring sources.

BEM IMPLEMENTATION

To solve the mechanical boundary conditions at the borehole wall, we represent the borehole wall as a distribution of secondary sources. The borehole is discretized into small cylindrical elements and each element is represented by four sources: a volume source generating wavefields diffracted into the fluid, V_i^f, a vertical, F_i^v, and radial, F_i^r, ring source acting on the elastic frame, and a volume injection ring source, F_i^e, acting on the pore fluid. The last three sources give rise to the poroelastic wavefields radiated into the formation. The density of the fictitious sources' wavefields are assumed to be constant on each element. To calculate an element's self interaction, the singular properties of the Green's functions need to be determined. The stress field for the dynamic Green's functions with a force on the elastic frame are also singular, while the displacement/relative flow for the dynamic Green's functions with a force on the pore fluid are singular. The contribution of the stress and displacement/relative flow singularities are determined analytically by integration of the static Green's functions over a half spherical surface when source and receiver coincide. The strength of each source is obtained by solving a linear system of equations that incorporate the mechanical boundary conditions at the borehole wall.

BOUNDARY CONDITION MATRIX

Within each element, the fluid-porous boundary conditions have to be satisfied (Deresiewicz and Skalak, 1963; Lovera, 1987; de la Cruz and Spanos, 1989).

- Normal displacement in the fluid matches the net normal displacement in the poroelastic medium.
- The stress in the fluid matches the bulk normal stress in the poroelastic medium.
- The stress in the fluid matches the stress in the fluid phase in the poroelastic medium.
- The poroelastic tangential bulk stress vanishes.

$$\begin{aligned} \left[u_r + w_r\right]|_{r=r_0^+} - u_r|_{r=r_0^-} &= 0 \\ \tau_{rr}|_{r=r_0^+} - \tau_{rr}|_{r=r_0^-} &= 0 \\ T_p|_{r=r_0^+} - \tau_{rr}|_{r=r_0^-} &= 0 \\ \tau_{rz}|_{r=r_0^+} &= 0 \end{aligned} \tag{1}$$

The boundary conditions are satisfied at the center of each element. The displacements, stresses, and pressure at the center of each element are due to the four fictitious sources on all elements. The indirect formulation is used to calculate the displacement at the

j-th element due to a source at the i-th element. At the j-th element, the boundary conditions become,

$$\begin{aligned}
\sum_{i=1}^{N_e} A_{ji}^f V_i^f + \sum_{i=1}^{N_e} A_{ji}^v F_i^v + \sum_{i=1}^{N_e} A_{ji}^r F_i^r + \sum_{i=1}^{N_e} A_{ji}^e F_i^e &= E_j^u \\
\sum_{i=1}^{N_e} B_{ji}^f V_i^f + \sum_{i=1}^{N_e} B_{ji}^v F_i^v + \sum_{i=1}^{N_e} B_{ji}^r F_i^r + \sum_{i=1}^{N_e} B_{ji}^e F_i^e &= E_j^{\tau_{rr}} \\
\sum_{i=1}^{N_e} C_{ji}^f V_i^f + \sum_{i=1}^{N_e} C_{ji}^v F_i^v + \sum_{i=1}^{N_e} C_{ji}^r F_i^r + \sum_{i=1}^{N_e} C_{ji}^e F_i^e &= E_j^{T_p} \\
\sum_{i=1}^{N_e} D_{ji}^v F_i^v + \sum_{i=1}^{N_e} D_{ji}^r F_i^r + \sum_{i=1}^{N_e} D_{ji}^e F_i^e &= E_j^{T_p}
\end{aligned} \tag{2}$$

where A_{ji}^f, A_{ji}^v and A_{ji}^r represent displacements at the j-th element due to the volume, vertical, radial, and explosive ring sources of unit strength at the i-th element, respectively. They are surface integrals of the appropriate Green's functions over the surfaces of the borehole. The B and C's are the radial stresses and the stresses in the fluid phase of the poroelastic formation at the j-th element due to sources at the i-th element. The D's are the tangential stresses at the j-th element due to sources at the i-th element. They are the surface integrals of the appropriate stress Green's functions. The E's are the fields excited at the j-th element.

The number of elements depends on the time window and the fastest wave speed. the element heights dz satisfy,

$$dz \leq \frac{min(c, \beta, \alpha)}{3f} \tag{3}$$

The number of elements, N_e is given by,

$$N_e = \frac{t_{max} \times max(c, \beta, \alpha)}{dz} = \frac{3f \times t_{max} \times max(c, \beta, \alpha)}{min(c, \beta, \alpha)} \tag{4}$$

with j ranging from 1 to N_e, $4 \times N_e$ equations are obtained that need to be solved for $4 \times N_e$ unknowns. The fields inside and outside the borehole can be calculated knowing these fictitious sources. The surface integration of the Green's functions is accomplished in two steps. The integrals are first transformed into wavenumber integrals, where the Sommerfeld integral representation to the function $\frac{e^{-ikR}}{4\pi R}$ is used. The wavenumber integration is then evaluated by the discrete wavenumber method. The scalar Green's functions g_i with $i = \beta \vee \alpha_1 \vee \alpha_2 \vee f$, are expressed in a horizontal wavenumber integral using,

$$g_i = \frac{-i}{4\pi} \int_0^\infty \frac{k}{\nu_i} J_0(kD) e^{-i\nu_i |z - z'|} dk \tag{5}$$

where $\nu_i = \sqrt{k_i^2 - k^2}$ and $D = \sqrt{r^2 + r_0^2 - 2rr_0\cos(\phi - \phi_0)}$. The spherical wavefront is now represented by infinitely many cylindrical wavefronts. Using the addition theorem for the zeroth order Bessel function (Watson, 1966)

$$J_0(kD) = \sum_{m=0}^{\infty} \epsilon_m J_m(kr) J_m(kr_0) \cos m(\phi - \phi_0), \tag{6}$$

one obtains

$$g_i = \frac{-i}{4\pi} \sum_{m=0}^{\infty} \epsilon_m \cos m(\phi - \phi_0) \int_0^{\infty} \frac{k}{\nu_i} J_m(kr) J_m(kr_0) e^{-i\nu_i |z - z'|} dk \tag{7}$$

where $\epsilon_m = 2 - \delta_{m0}$, and J_m is the m-th order Bessel function of the first kind. The integrand of the above wavenumber integral simplifies when the surface integration $r_0 d\phi_0 dz$ is performed, due to the orthogonality of the sine and cosine functions over the integration range 0 to 2 π. The final result of this integration represents the response of a circular ring source. The dz part of the surface integral can be carried out analytically through the integration of the ring source results over z'. Since the integral over element height depends on horizontal wavenumbers, its evaluation must precede the wavenumber integration. The integration over the source element coordinate z' is of two types, an integral of a complex exponential and an integral of a sign function multiplied by a complex exponential function. Both integral types can be performed analytically.

$$\int_{z_l}^{z_h} e^{-i\nu(z-z')} dz' = \begin{cases} \frac{1}{i\nu}\left[e^{-i\nu(z-z_h)} - e^{-i\nu(z-z_l)}\right] & for \;\; z > z_h; \\ \frac{-1}{i\nu}\left[e^{-i\nu(z_h-z)} - e^{-i\nu(z_l-z)}\right] & for \;\; z < z_l; \\ \frac{-1}{i\nu}\left[e^{-i\nu(z_h-z)} + e^{-i\nu(z-z_l)} - 2\right] & for \;\; z_l < z < z_h. \end{cases} \tag{8}$$

and,

$$\int_{z_l}^{z_h} sgn(z - z') e^{-i\nu(z-z')} dz' = \begin{cases} \frac{1}{i\nu}\left[e^{-i\nu(z-z_h)} - e^{-i\nu(z-z_l)}\right] & for \;\; z > z_h; \\ \frac{1}{i\nu}\left[e^{-i\nu(z_h-z)} - e^{-i\nu(z_l-z)}\right] & for \;\; z < z_l; \\ \frac{-1}{i\nu}\left[e^{-i\nu(z_h-z)} - e^{-i\nu(z-z_l)}\right] & z_l < z < z_h. \end{cases} \tag{9}$$

The element surface integration of the Green's function reduces to a horizontal wavenumber integral. The field integrals are evaluated by the discrete summation, the so-called Discrete Wavenumber Method (Bouchon and Aki, 1977). The discretization of the radial wavenumber k in cylindrical coordinates introduces periodicity into the source distribution. The original single source problem changes after discretization into periodic concentric sources around the original source. The periodicity of these sources, or the distance between two adjacent circular sources, L, is related to the discretization interval of the wavenumber, Δk, by the sampling relation,

$$L = \frac{2\pi}{\Delta k}. \tag{10}$$

L, and therefore Δk, is determined by assuming a receiver located at $x_r = (r_0, z_0)$ and a source at $x_s = (0, z_s)$ on the symmetry axes of the medium configuration. Given the time window to record radiated waves from 0 to t_{max}, "pseudo" waves radiated from the periodic sources are not allowed to enter this time window. This requirement is,

$$\sqrt{(L - r_0)^2 + (z_0 - z_s)^2} > v_{fastest} t_{max} \tag{11}$$

or

$$L > r_0 + \sqrt{v_{fastest}^2 t_{max}^2 - (z_0 - z_s)^2}. \tag{12}$$

The sampling equation becomes now,

$$\Delta k < \frac{2\pi}{r_0 + \sqrt{v_{fastest}^2 t_{max}^2 - (z_0 - z_s)^2}}. \tag{13}$$

The above equation is the criterion for choosing the sample rate for the discrete wavenumber summation.

To perform the summation, the singularities of the integrands must be removed from the real k axes. This is done by adding a small imaginary part to the real frequency (analytic continuation into the complex plane), i.e. $\omega = \omega_R + i\omega_I$ with $\omega_I > 0$. If $e^{i\omega t}$ was used in the time to frequency transformation there would be a minus sign for the imaginary part of the frequency. The effect of complex frequency moves the singularities into the first and third quadrant of the complex k-plane. The use of complex frequency has the effect of smoothing the spectrum and enhancing the first motions relative to later arrivals. This effective attenuation is used to minimize the influence of the neighboring fictitious sources introduced by discrete k. The effect of the imaginary part of the frequency can be removed from the final time domain solution by inverse complex Fourier transform with complex frequency, using the same imaginary part in the argument of the exponential function in the Fourier transform. The magnitude of the imaginary part is usually chosen to be,

$$\omega_I = \frac{\pi}{t_{max}}. \tag{14}$$

Larger ω_I increases the attenuation for later arrivals, but also magnifies the numerical noise for late times. If ω_I is chosen too small, attenuation may not be large enough to damp out the arrivals from the fictitious sources.

SINGULARITIES WHEN SOURCE AND RECEIVER COINCIDE

In boundary integral or boundary element techniques, integration of the Green's function over boundary surfaces is necessary. When receiver and source position coincide, the Green's function becomes singular. The displacement and relative flow Green's function have first order singularities which are removable when integrated over the surface. The stress Green's function has a second order singularity and the surface integral is

not defined. Here the principle value of the improper integral has to be calculated. The contribution of this second order singularity to the integral can be evaluated analytically. When the receiver and the source approach each other, the surface integral of the dynamic Green's functions can be regularized using the static Green's function (Kupradze, 1963). The improper integral of the dynamic Green's function is reduced to the integration of the static Green's functions over a half spherical surface around the source/receiver point. First the displacement and stress field components are calculated using the static Green's functions, equations (A-23) and (A-29) for a vertical point force.

$$u_x = \frac{[HM - C^2 - GM]}{8\pi G\,[HM - C^2]} \left[\frac{(z - z^{'})(x - x^{'})}{R^3}\right] \tag{15}$$

$$u_y = \frac{[HM - C^2 - GM]}{8\pi G\,[HM - C^2]} \left[\frac{(z - z^{'})(y - y^{'})}{R^3}\right] \tag{16}$$

$$u_z = \frac{1}{4\pi GR} - \frac{[HM - C^2 - GM]}{8\pi G\,[HM - C^2]} \left[\frac{R^2 - (z - z^{'})}{R^3}\right]. \tag{17}$$

Notice that the displacements have a first order singularity when $\mathbf{x} \rightarrow \mathbf{x}^{'}$. The stress in a poroelastic medium along the $\hat{z}$ direction on a surface with the normal in the $\hat{x}$ direction is,

$$\begin{aligned} \tau_{xz} &= G\left[\frac{\partial}{\partial x}u_z + \frac{\partial}{\partial z}u_x\right] \\ &= \frac{x - x^{'}}{4\pi GR^3} - \frac{[HM - C^2 - GM]}{8\pi G\,[HM - C^2]} \left[\frac{2R^3(x - x^{'}) - 3R(x - x^{'})(z - z^{'})^2}{R^6}\right]. \end{aligned} \tag{18}$$

The stress has a second order singularity when the source and receiver position coincide at R = 0. The stress integrated over a surface results in a finite value. The magnitude of this value can be obtained by integrating τ_{xz} over all possible $dydz$ surrounding the source. This integration can be replaced by integration over a half sphere around the source point. This surface is defined by $x - x^{'} = R\sin(\theta)\cos(\phi)$, $y - y^{'} = R\sin(\theta)\sin(\phi)$, $z - z^{'} = R\cos(\theta)$. Then the surface mapping between $dydz$ and the differential spherical surface becomes, $dydz\sin(\theta)\cos(\phi) = R^2\sin(\theta)d\theta d\phi$. Integrating the stress, τ_{xz} yields,

$$\begin{aligned} \int \tau_{xz}dydz &= \left[\frac{-1}{4\pi} + \frac{HM - C^2 - GM}{4\pi\,(HM - C^2)}\right] \int_{\pi/2}^{\pi/2} d\phi \int_0^{\pi} \sin(\theta)d\theta \\ &- \frac{3\,(HM - C^2 - GM)}{4\pi\,(HM - C^2)} \int_{\pi/2}^{\pi/2} d\phi \int_0^{\pi} \sin(\theta)\cos^2(\theta)d\theta = -\frac{1}{2}. \end{aligned} \tag{19}$$

For a point force in the $\hat{x}$ direction, the displacement and relative flow components are,

$$u_x = \frac{1}{4\pi GR} - \frac{HM - C^2 - GM}{8\pi G\,(HM - C^2)} \left[\frac{R^2 - (x - x^{'})}{R^3}\right] \tag{20}$$

$$u_y = \frac{HM - C^2 - GM}{8\pi G\,(HM - C^2)} \left[\frac{(x - x')(y - y')}{R^3}\right] \tag{21}$$

$$u_z = \frac{HM - C^2 - GM}{8\pi G\,(HM - C^2)} \left[\frac{(x - x')(z - z')}{R^3}\right] \tag{22}$$

$$w_x = \frac{-1}{4\pi GR} + \frac{HM - C^2 - GC}{8\pi G\,(HM - C^2)} \left[\frac{R^2 - (x - x')}{R^3}\right] \tag{23}$$

$$w_y = -\frac{HM - C^2 - GC}{8\pi G\,(HM - C^2)} \left[\frac{(x - x')(y - y')}{R^3}\right] \tag{24}$$

$$w_z = -\frac{HM - C^2 - GC}{8\pi G\,(HM - C^2)} \left[\frac{(x - x')(z - z')}{R^3}\right]. \tag{25}$$

The normal stress is given by,

$$\tau_{xx} = H\frac{\partial}{\partial x}u_x + (H-2G)\frac{\partial}{\partial y}u_y + (H-2G)\frac{\partial}{\partial z}u_z + C\left(\frac{\partial}{\partial x}w_x + \frac{\partial}{\partial y}w_y + \frac{\partial}{\partial z}w_z\right). \tag{26}$$

Integrating the stress, τ_{xx} yields,

$$\begin{aligned}
\int \tau_{xx}\,dydz \;=\; & \left[\frac{-1}{4\pi G} + \frac{3H(HM - C^2 - GM)}{8\pi G(HM - C^2)} + \frac{2(H - 2G)(HM - C^2 - GM)}{8\pi G(HM - C^2)}\right. \\
& + \left.\frac{C}{4\pi G} - \frac{5C(HM - C^2 - GC)}{8\pi G(HM - C^2)}\right] \int_{\pi/2}^{\pi/2} d\phi \int_0^{\pi} \sin(\theta)\,d\theta \\
& + \left[\frac{-3(H - 2G)(HM - C^2 - GM)}{8\pi G(HM - C^2)} + \frac{3C(HM - C^2 - GC)}{8\pi G(HM - C^2)}\right] \\
& \times \int_{-\pi/2}^{\pi/2}\int_0^{\pi} \left[\sin^3(\theta)\sin^2(\phi) + \sin^2(\theta)\cos(\theta)\right] d\phi\,d\theta \\
& + \left[\frac{-3H(HM - C^2 - GM)}{8\pi G(HM - C^2)} + \frac{3C(HM - C^2 - GC)}{8\pi G(HM - C^2)}\right] \\
& \times \int_{-\pi/2}^{\pi/2}\int_0^{\pi} \sin^3(\theta)\cos^2(\phi)\,d\phi\,d\theta = -\frac{1}{2}.
\end{aligned} \tag{27}$$

The point source potential and pressure, describing the acoustic behavior in the fluid phase of the poroelastic solid, have first order singularities when source and receiver coincide. These singularities, however, are removable; the integration of potential and pressure over an infinitesimal surface around $\mathbf{x} = \mathbf{x}'$ approaches zero when the surface shrinks to a point. The point displacement has a second order singularity, since the gradient of the Green's function is taken. Integration of the displacement over a spherical

surface centered at $\mathbf{x} = \mathbf{x}'$ approaches a constant as the radius of the sphere shrinks to zero.

Using equations (A-16) and (A-17), the x component of the relative flow caused by a pressure source can be obtained. Integrating the relative flow, w_x, over all possible $dydz$ surrounding the source yields,

$$\begin{aligned}\int w_x dydz &= \lim_{R\to 0}\left[\int_{-\frac{\pi}{2}}^{\frac{\pi}{2}} d\phi \int_0^{\pi}\left(\Lambda_1(ik_{\alpha 1}R-1)\frac{ik_{\alpha 1}R}{4\pi}+\right.\right. \\ &\qquad \left.\left.\Lambda_2(ik_{\alpha 2}R-1)\frac{ik_{\alpha 2}R}{4\pi}\right)\sin(\theta)\right] d\theta \qquad (28)\\ &= -\frac{1}{2}\left[\Lambda_1+\Lambda_2\right] = \frac{1}{2}\frac{H}{HM-C^2}. \qquad (29)\end{aligned}$$

The x component of the bulk displacement caused by a pressure source is obtained by taking the divergence of equation (A-29). Integrating the displacement, u_x, over all possible $dydz$ surrounding the source yields,

$$\int u_x dydz = \int_{-\frac{\pi}{2}}^{\frac{\pi}{2}} d\phi \int_0^{\pi}\left(\frac{C}{4\pi\left[HM-C^2\right]}\sin(\theta)\right) d\theta = -\frac{1}{2}\frac{C}{HM-C^2}. \qquad (30)$$

To obtain the jump in the fluid displacement due to a **volume injection source**, the displacement potential Φ [dim m^2] will be introduced. The fluid displacement is related to the displacement potential as follows,

$$\underline{u}^{(f)} = \nabla\Phi = C\underline{u} + M\underline{w} \qquad (31)$$

$$\int u_x^{(f)} dydz = C\int u_x dydz + M\int w_x dydz = \frac{1}{2}. \qquad (32)$$

RING SOURCE RESULTS IN POROELASTIC MEDIA

In this section the displacements, relative flows and stresses, and pressures of the different ring sources are obtained by integrating the appropriate Green's functions directly over a ring.

Vertical Ring Source

For a vertical source located at (r_0, z'), $F^v(x) = \hat{z}\delta(z-z')\delta(r-r_0)$. The integration over the angle ϕ_0 is non zero only for $m = 0$, due to the orthogonality of the set $\{1, \cos\phi, \cos 2\phi, ...\}$. Substituting equation (A-2) into displacement Green's function (A-1) and using equation (7) to rewrite the scalar Green's functions, the displacements at point (r, z) due to a ring of unit vertical forces at $x_0 = (r_0, z')$ are obtained. When

the relative flow Green's function in equation (A-7) is used instead, the relative flows at point (r,z) due to a ring of unit vertical forces at $x_0=(r_0,z')$ are obtained.

$$\begin{aligned} u_r &= -sgn(z-z')\frac{r_0}{2}\int_0^\infty J_1(kr)J_0(kr_0) \\ &\times \left[U^r_\beta e^{-i\nu_\beta|z-z'|}+U^r_{\alpha_1}e^{-i\nu_{\alpha_1}|z-z'|}+U^r_{\alpha_2}e^{-i\nu_{\alpha_2}|z-z'|}\right]dk \end{aligned} \tag{33}$$

$$u_z=-i\frac{r_0}{2}\int_0^\infty kJ_0(kr)J_0(kr_0)\left[U^z_\beta e^{-i\nu_\beta|z-z'|}+U^z_{\alpha_1}e^{-i\nu_{\alpha_1}|z-z'|}+U^z_{\alpha_2}e^{-i\nu_{\alpha_2}|z-z'|}\right]dk \tag{34}$$

$$\begin{aligned} w_r &= -sgn(z-z')\frac{r_0}{2}\int_0^\infty J_1(kr)J_0(kr_0) \\ &\times \left[W^r_\beta e^{-i\nu_\beta|z-z'|}+W^r_{\alpha_1}e^{-i\nu_{\alpha_1}|z-z'|}+W^r_{\alpha_2}e^{-i\nu_{\alpha_2}|z-z'|}\right]dk \end{aligned} \tag{35}$$

$$w_z=-i\frac{r_0}{2}\int_0^\infty kJ_0(kr)J_0(kr_0)\left[W^z_\beta e^{-i\nu_\beta|z-z'|}+W^z_{\alpha_1}e^{-i\nu_{\alpha_1}|z-z'|}+W^z_{\alpha_2}e^{-i\nu_{\alpha_2}|z-z'|}\right]dk. \tag{36}$$

Substituting equations (33)- (36) into the stress equation in cylindrical coordinates and incorporating the static contribution to τ_{rz}, when source and receiver position coincide, the stresses are obtained at $x=(r,z)$.

$$\begin{aligned} \tau_{rr} &= -sgn(z-z')\frac{r_0}{2}\int_0^\infty J_0(kr_0)I_1dk \\ I_1 &= \sum_{p=\beta,\alpha_1,\alpha_2}\left[\left(HkU^r_p+CkW^r_p+(H-2G)\nu_pkU^z_p+C\nu_pkW^z_p\right)J_0(kr)\right. \\ &- \left.2GU^r_p\frac{J_1(kr)}{r}\right]e^{-i\nu_p|z-z'|} \end{aligned} \tag{37}$$

$$\begin{aligned} \tau_{rz} &= -\frac{1}{2}\delta(z-z')+iG\frac{r_0}{2}\int_0^\infty kJ_1(kr)J_0(kr_0)I_2dk \\ I_2 &= 2k\left[U^z_\beta-\frac{1}{G\nu_\beta}\right]e^{-i\nu_\beta|z-z'|}+2kU^z_{\alpha_1}e^{-i\nu_{\alpha_1}|z-z'|}+2kU^z_{\alpha_2}e^{-i\nu_{\alpha_2}|z-z'|} \end{aligned} \tag{38}$$

$$\begin{aligned} \tau_{zz} &= -sgn(z-z')\frac{r_0}{2}\int_0^\infty J_0(kr)J_0(kr_0)I_3dk \\ I_3 &= \sum_{p=\beta,\alpha_1,\alpha_2}\left[\left((H-2G)kU^r_p+CkW^r_p+H\nu_pkU^z_p+C\nu_pkW^z_p\right)\right]e^{-i\nu_p|z-z'|} \end{aligned} \tag{39}$$

$$\begin{aligned} T_p &= -sgn(z-z')\frac{r_0}{2}\int_0^\infty kJ_0(kr)J_0(kr_0)I_4dk \\ I_4 &= \sum_{p=\beta,\alpha_1,\alpha_2}\left[C(U^r_p+\nu_pU^z_p)+M(W^r_p+\nu_pW^z_p)\right]e^{-i\nu_p|z-z'|} \end{aligned} \tag{40}$$

where the introduced variables, $W^r_\beta, W^r_{\alpha_1}, W^r_{\alpha_2}, U^r_\beta, U^r_{\alpha_1}, U^r_{\alpha_2}, W^z_\beta, W^z_{\alpha_1,\alpha_2}, U^z_\beta, U^z_{\alpha_1}, U^z_{\alpha_2}$ are defined as,

$$W^r_\beta = \left[\Pi B^*(ws)-\Delta B(ws)\right]k^2, \quad U^r_\beta=\left[\Xi B^*(us)-\Gamma B(us)\right]k^2 \tag{41}$$

$$W^r_{\alpha_1} = [\Pi A^*_1(ws) - \Delta A_1(ws)]\, k^2, \quad U^r_{\alpha_1} = [\Xi A^*_1(us) - \Gamma A_1(us)]\, k^2 \tag{42}$$

$$W^r_{\alpha_2} = [\Pi A^*_2(ws) - \Delta A_2(ws)]\, k^2, \quad U^r_{\alpha_2} = [\Xi A^*_2(us) - \Gamma A_2(us)]\, k^2 \tag{43}$$

$$W^z_\beta = -\frac{\rho_f}{\rho_E}\frac{1}{G\nu_\beta} - \Delta B(ws)\nu_\beta + \Pi B^*(ws)\nu_\beta, \tag{44}$$

$$U^z_\beta = \frac{1}{G\nu_\beta} - \Gamma B(us)\nu_\beta + \Xi B^*(us)\nu_\beta \tag{45}$$

$$W^z_{\alpha_1} = -\Delta A_1(ws)\nu_{\alpha_1} + \Pi A^*_1(ws)\nu_{\alpha_1}, \quad U^z_{\alpha_1} = -\Gamma A_1(us)\nu_{\alpha_1} + \Xi A^*_1(us)\nu_{\alpha_1} \tag{46}$$

$$W^z_{\alpha_2} = -\Delta A_2(ws)\nu_{\alpha_2} + \Pi A^*_2(ws)\nu_{\alpha_2}, \quad U^z_{\alpha_2} = -\Gamma A_2(us)\nu_{\alpha_2} + \Xi A^*_2(us)\nu_{\alpha_2} \tag{47}$$

Variables $A_q(ws), A^*_q(ws), B_q(ws), B^*_q(ws)$ are defined in equations (A-9) and (A-11) and variables $A_q(us), A^*_q(us), B_q(us), B^*_q(us)$ are defined in equations (A-3) and (A-5), with $q = 1 \vee 2$, with,

$$\Gamma = G - \frac{1}{M}\left[HM - C^2\right] \tag{48}$$

$$\Xi = -2\omega^2\rho_f C + M\omega^2\frac{\rho_f^2}{\rho_E} + \frac{C^2}{M}\omega^2\rho_E \tag{49}$$

$$\Delta = \frac{1}{C}\left[HM - C^2\right] - G\frac{\rho_E}{\rho_f} \tag{50}$$

$$\Pi = \frac{HM}{C}\omega^2\rho_f + C\omega^2\frac{\rho_B\rho_E}{\rho_f} - H\omega^2\rho_E - M\omega^2\rho_B \tag{51}$$

Radial Ring Source

For a radial ring source $F^r(x) = \left[\hat{r}\cos(\phi - \phi_0) - \hat{\phi}\sin(\phi - \phi_0)\right]\delta(r - r_0)\delta(z - z')$. Using the displacement Green's function, (A-1), and the scalar Green's functions, equations (A-2) and (A-6), which are rewritten using equation (7) and the orthogonality property in the integration over angle ϕ_0, the displacements at (r, z) due to a ring of unit radial forces at $x' = (r_0, z')$ are obtained. When the relative flow Green's function, equation (A-7), and the scalar Green's functions, equations (A-8) and (A-12), are used instead, the relative flow vector components (r, z) due to a ring of unit radial forces at $x' = (r_0, z')$ are obtained.

$$u_r = i\frac{r_0}{2}\int_0^\infty J_1(kr)J_1(kr_0)\left[U^r_\beta e^{-i\nu_\beta|z-z'|} + U^r_{\alpha_1}e^{-i\nu_{\alpha_1}|z-z'|} + U^r_{\alpha_2}e^{-i\nu_{\alpha_2}|z-z'|}\right]dk \tag{52}$$

$$u_z = sgn(z - z')\frac{r_0}{2}\int_0^\infty kJ_0(kr)J_1(kr_0) \times \left[U^z_\beta e^{-i\nu_\beta|z-z'|} + U^z_{\alpha_1}e^{-i\nu_{\alpha_1}|z-z'|} + U^z_{\alpha_2}e^{-i\nu_{\alpha_2}|z-z'|}\right]dk \tag{53}$$

$$w_r = i\frac{r_0}{2}\int_0^\infty J_1(kr)J_1(kr_0)\left[W^r_\beta e^{-i\nu_\beta|z-z'|} + W^r_{\alpha_1}e^{-i\nu_{\alpha_1}|z-z'|} + W^r_{\alpha_2}e^{-i\nu_{\alpha_2}|z-z'|}\right]dk \tag{54}$$

$$w_z = sgn(z-z')\frac{r_0}{2}\int_0^\infty kJ_0(kr)J_1(kr_0) \times \left[W^z_\beta e^{-i\nu_\beta|z-z'|} + W^z_{\alpha_1} e^{-i\nu_{\alpha_1}|z-z'|} + W^z_{\alpha_2} e^{-i\nu_{\alpha_2}|z-z'|}\right] dk \quad (55)$$

Substituting equations (52)– (55) into the stress equation in cylindrical coordinates and incorporating the static contribution to τ_{rr}, when source and receiver position coincide, the stresses are obtained at $x = (r, z)$. When equations (52)– (55) are substituted into the pressure equation in cylindrical coordinates, the fluid traction is obtained at $x = (r, z)$.

$$\begin{aligned}
\tau_{rr} &= -\frac{1}{2}\delta(z-z') + i\frac{r_0}{2}\int_0^\infty J_1(kr_0)I_1 dk \\
I_1 &= \sum_{p=\beta,\alpha_1,\alpha_2}\left[\left(HkU^r_p + CkW^r_p - (H-2G)k\nu_p U^z_p - Ck\nu_p W^z_p\right)J_0(kr)\right. \\
&- \left. 2GU^r_p\frac{J_1(kr)}{r}\right] e^{-i\nu_p|z-z'|} \quad (56) \\
\tau_{rz} &= sgn(z-z')\frac{r_0}{2}\int_0^\infty J_1(kr)J_1(kr_0)I_2 dk \\
I_2 &= G\left[(\nu_\beta U^r_\beta - k^2U^z_\beta)e^{-i\nu_\beta|z-z'|} + \right. \\
&\left. (\nu_{\alpha_1}U^r_{\alpha_1} - k^2U^z_{\alpha_1})e^{-i\nu_{\alpha_1}|z-z'|} + (\nu_{\alpha_2}U^r_{\alpha_2} - k^2U^z_{\alpha_2})e^{-i\nu_{\alpha_2}|z-z'|}\right] \quad (57) \\
\tau_{zz} &= i\frac{r_0}{2}\int_0^\infty J_0(kr)J_1(kr_0)I_3 dk \\
I_3 &= \sum_{p=\beta,\alpha_1,\alpha_2}\left[(H-2G)kU^r_p + CkW^r_p - Hk\nu_p U^z_p - Ck\nu_p W^z_i\right] e^{-i\nu_p|z-z'|} \quad (58) \\
T_p &= i\frac{r_0}{2}\int_0^\infty J_0(kr)J_1(kr_0)I_4 dk \\
I_4 &= \sum_{i=\beta,\alpha_1,\alpha_2}\left[C(kU^r_p - \nu_p kU^z_p) + M(kW^r_p - \nu_p kW^z_p\right] e^{-i\nu_p|z-z'|} \quad (59)
\end{aligned}$$

where the introduced variables, $W^r_\beta, W^r_{\alpha_1}, W^r_{\alpha_2}, U^r_\beta, U^r_{\alpha_1}, U^r_{\alpha_2}, W^z_\beta, W^z_{\alpha_1,\alpha_2}, U^z_\beta, U^z_{\alpha_1}, U^z_{\alpha_2}$ are defined as,

$$\begin{aligned}
W^r_\beta &= \frac{\rho_f}{\rho_E}\frac{k}{G\nu_\beta} + B(ws)\Delta\frac{k^3}{\nu_\beta} - B^*(ws)\Pi\frac{k^3}{\nu_\beta},\ U^r_\beta = -\frac{k}{\nu_\beta G} + \Gamma B(us)\frac{k^3}{\nu_\beta} - \Xi B^*(us)\frac{k^3}{\nu_\beta} \quad (59) \\
W^r_{\alpha_1} &= A_1(ws)\Delta\frac{k^3}{\nu_{\alpha_1}} - A^*_1(ws)\Pi\frac{k^3}{\nu_{\alpha_1}},\quad U^r_{\alpha_1} = \Gamma A_1(us)\frac{k^3}{\nu_{\alpha_1}} - \Xi A^*_1(us)\frac{k^3}{\nu_{\alpha_1}} \quad (60) \\
W^r_{\alpha_2} &= A_2(ws)\Delta\frac{k^3}{\nu_{\alpha_2}} - A^*_2(ws)\Pi\frac{k^3}{\nu_{\alpha_2}},\quad U^r_{\alpha_2} = \Gamma A_2(us)\frac{k^3}{\nu_{\alpha_2}} - \Xi A^*_2(us)\frac{k^3}{\nu_{\alpha_2}} \quad (61) \\
W^z_\beta &= [\Pi B^*(ws) - \Delta B(ws)]\,k,\quad U^z_\beta = [\Xi B^*(us) - \Gamma B(us)]\,k \quad (62) \\
W^z_{\alpha_1} &= [\Pi A^*_1(ws) - \Delta A_1(ws)]\,k,\quad U^z_{\alpha_1} = [\Xi A^*_1(us) - \Gamma A_1(us)]\,k \quad (63) \\
W^z_{\alpha_2} &= [\Pi A^*_2(ws) - \Delta A_2(ws)]\,k,\quad U^z_{\alpha_2} = [\Xi A^*_1(us) - \Gamma A_2(us)]\,k. \quad (64)
\end{aligned}$$

$$W^z_\beta = [\Pi B^*(ws) - \Delta B(ws)]\,k, \quad U^z_\beta = [\Xi B^*(us) - \Gamma B(us)]\,k \tag{64}$$
$$W^z_{\alpha_1} = [\Pi A^*_1(ws) - \Delta A_1(ws)]\,k, \quad U^z_{\alpha_1} = [\Xi A^*_1(us) - \Gamma A_1(us)]\,k \tag{65}$$
$$W^z_{\alpha_2} = [\Pi A^*_2(ws) - \Delta A_2(ws)]\,k, \quad U^z_{\alpha_2} = [\Xi A^*_1(us) - \Gamma A_2(us)]\,k. \tag{66}$$

Variables $A_q(ws), A^*_q(ws), B_q(ws), B^*_q(ws)$ are defined in equations (A-9) and (A-11) and variables $A_q(us), A^*_q(us), B_q(us), B^*_q(us)$ are defined in equations (A-3) and (A-5), with $q = 1 \vee 2$, with variables, Γ, Ξ, Δ, Π defined in equation (48).

Explosive Ring Source in Porous Medium

For an explosive source located at (r_0, z'), $F^e(x) = V\delta(z - z')\delta(r - r_0)$. Using the displacement Green's function, (A-13), and the scalar Green's function, equation (A-14), which are rewritten using equation (7), and the orthogonality property in the integration over angle ϕ_0, the displacements at (r, z) due to a ring of explosive point forces at $x' = (r_0, z')$ are obtained. When the relative flow Green's function, equation (A-16), and the scalar Green's function, equation (A-17), are used instead, the relative flow vector components (r, z) due to a ring of explosive point forces at $x' = (r_0, z')$ are obtained.

$$\begin{aligned} u_r &= -\frac{1}{2}\frac{C}{HM - C^2}\delta(z - z') \\ &+ i\frac{r_0}{2}\int_0^\infty k^2 J_1(kr)J_0(kr_0)\left[U^e_{\alpha_1} e^{-i\nu_{\alpha_1}|z-z'|} + U^e_{\alpha_2} e^{-i\nu_{\alpha_2}|z-z'|}\right] dk \end{aligned} \tag{67}$$

$$u_z = -sgn(z - z')\frac{r_0}{2}\int_0^\infty kJ_0(kr)J_0(kr_0)\left[\nu_{\alpha_1} U^e_{\alpha_1} e^{-i\nu_{\alpha_1}|z-z'|} + \nu_{\alpha_2} U^e_{\alpha_2} e^{-i\nu_{\alpha_2}|z-z'|}\right] dk \tag{68}$$

$$\begin{aligned} w_r &= \frac{1}{2}\frac{M}{HM - C^2}\delta(z - z') \\ &+ i\frac{r_0}{2}\int_0^\infty J_1(kr)J_0(kr_0)\left[\Lambda_1\frac{k^2}{\nu_{\alpha_1}} e^{-i\nu_{\alpha_1}|z-z'|} + \Lambda_2\frac{k^2}{\nu_{\alpha_2}} e^{-i\nu_{\alpha_2}|z-z'|}\right] dk \end{aligned} \tag{69}$$

$$w_z = -sgn(z - z')\frac{r_0}{2}\int_0^\infty kJ_0(kr)J_0(kr_0)\left[\Lambda_1 e^{-i\nu_{\alpha_1}|z-z'|} + \Lambda_2 e^{-i\nu_{\alpha_2}|z-z'|}\right] dk. \tag{70}$$

Substituting equations (67)– (70) into the stress equation in cylindrical coordinates yields the stresses at $x = (r, z)$. When equations (52)– (70) are substituted into the pressure equation in cylindrical coordinates, the fluid traction is obtained at $x = (r, z)$.

$$\begin{aligned} \tau_{rr} &= i\frac{r_0}{2}\int_0^\infty J_0(kr_0)I_1\,dk \\ I_1 &= \sum_{p=\alpha_1,\alpha_2}\left[\left(Hk^2U^e_p + (H - 2G)\nu_p^2 kU^e_p + C\Lambda_p\left(\frac{k^3}{\nu_p} + k\nu_p\right)\right)J_0(kr)\right. \\ &- \left. 2GU^e_p k^2\frac{J_1(kr)}{r}\right] e^{-i\nu_p|z-z'|} \end{aligned} \tag{71}$$

$$
\begin{aligned}
\tau_{rz} &= sgn(z-z^{'})r_0\int_0^\infty kJ_0(kr)J_0(kr_0)I_2dk \\
I_2 &= \sum_{p=\alpha_1,\alpha_2} G\nu_p k U_p^e e^{-i\nu_{\alpha_1}|z-z^{'}|} \qquad (72)\\
\tau_{zz} &= i\frac{r_0}{2}\int_0^\infty kJ_0(kr)J_0(kr_0)I_3dk \\
I_3 &= \left[H\nu_{\alpha_1}^2U_{\alpha_1}^e + (H-2G)k^2U_{\alpha_1}^e + C\Lambda_1\left(\frac{k^2}{\nu_{\alpha_1}}+\nu_{\alpha_1}\right)\right]e^{-i\nu_{\alpha_1}|z-z^{'}|} \\
&+ \left[H\nu_{\alpha_2}^2U_{\alpha_2}^e + (H-2G)k^2U_{\alpha_2}^e + C\Lambda_2\left(\frac{k^2}{\nu_{\alpha_2}}+\nu_{\alpha_2}\right)\right]e^{-i\nu_{\alpha_2}|z-z^{'}|} \qquad (73)\\
T_p &= i\frac{r_0}{2}\int_0^\infty J_0(kr)J_0(kr_0)I_4dk \\
I_4 &= \left[C\left(k^2+\nu_{\alpha_1}^2\right)kU_{\alpha_1}^e + M\Lambda_1\left(\frac{k^3}{\nu_{\alpha_1}}+k\nu_{\alpha_1}\right)\right]e^{-i\nu_{\alpha_1}|z-z^{'}|} \\
&+ \left[C\left(k^2+\nu_{\alpha_2}^2\right)kU_{\alpha_2}^e + M\Lambda_2\left(\frac{k^3}{\nu_{\alpha_2}}+k\nu_{\alpha_2}\right)\right]e^{-i\nu_{\alpha_2}|z-z^{'}|} \qquad (74)
\end{aligned}
$$

where the introduced variables $U_{\alpha_1}^e, U_{\alpha_1}^e$ are defined as,

$$U_{\alpha_1}^e = -\left[\Upsilon+\Omega\right]\frac{k_{\alpha_1}^2}{\nu_{\alpha_1}}\left(A_1(wf)+A_1^*(wf)\right) \qquad (75)$$

$$U_{\alpha_2}^e = -\left[\Upsilon+\Omega\right]\frac{k_{\alpha_2}^2}{\nu_{\alpha_2}}\left(A_2(wf)+A_2^*(wf)\right). \qquad (76)$$

Variables $A_q(wf), A_q^*(wf)$ are defined in equations (A-18) and (A-17), with $q = 1 \vee 2$, with,

$$\Upsilon = \frac{1}{C}\left[C^2 - HM + GC\frac{\rho_E}{\rho_f}\right] \qquad (77)$$

$$\Omega = \frac{HM}{C}\omega^2\rho_f + C\omega^2\frac{\rho_B\rho_E}{\rho_f} - H\omega^2\rho_E - M\omega^2\rho_B. \qquad (78)$$

Explosive Ring Source in Fluid

For an explosive source ring, the displacement potential is obtained by integrating $g(x,x^{'}) = e^{-ik_f|x-x^{'}|}/(4\pi|x-x^{'}|)$ with respect to angle ϕ,

$$\phi = -\frac{ir_0}{2}\int_0^\infty \frac{k}{\nu_f}J_0(kr)J_0(kr_0)e^{-i\nu_f|z-z^{'}|}dk. \qquad (79)$$

The fluid displacement components are obtained by taking the derivative with respect of r and z of equation (79).

$$u_r = -\frac{1}{2}\delta(z-z^{'}) + \frac{ir_0}{2}\int_0^\infty \frac{k^2}{\nu_f}J_1(kr)J_0(kr_0)e^{-i\nu_f|z-z^{'}|}dk$$

$$u_z = -sgn(z-z')\frac{r_0}{2}\int_0^\infty kJ_0(kr)J_0(kr_0)e^{-i\nu_f|z-z'|}dk \quad (80)$$

The stresses in the fluid, which are the negations of the fluid pressure, are,

$$\begin{aligned}\tau_{rr} &= \rho\omega^2\frac{ir_0}{2}\int_0^\infty \frac{k}{\nu_f}J_0(kr)J_0(kr_0)e^{-i\nu_f|z-z'|}dk \\ \tau_{zz} &= \tau_{rr} \\ \tau_{rz} &= 0. \end{aligned} \quad (81)$$

Explosive Volume Source in an Open Borehole

The driving initial data for an explosive source at the center of a fluid filled borehole at the boundary wall are,

$$u_r = \frac{V_s}{4\pi}i\int_0^\infty \frac{k^2}{\nu_f}J_1(kr_0)e^{-i\nu_f|z-z_s|}dk$$

$$\tau_{rr} = \rho\omega^2\frac{V_s}{4\pi}i\int_0^\infty \frac{k}{\nu_f}J_0(kr_0)e^{-i\nu_f|z-z_s|}dk \quad (82)$$

$$\tau_{rz} = 0 \quad (83)$$

where the vertical position of the source and the element position are denoted by z_s and z, respectively. The strength of the volume source $V_s[dim\ \ m^3]$ is taken 1600 cm^3.

RING SOURCES IN HORIZONTALLY LAYERED POROELASTIC MEDIA

To include the ring sources into layered media, we first manipulate the wavefield components that will be continous across the horizontal boundaries in the following form:

$$\begin{aligned} u_1(r,z) &= \int_0^\infty \hat{u}_1(k,z)kJ_0(kr)dk \\ u_z(r,z) &= \int_0^\infty \hat{u}_z(k,z)kJ_0(kr)dk \\ w_z(r,z) &= \int_0^\infty \hat{w}_z(k,z)kJ_0(kr)dk \\ \tau_1(r,z) &= \int_0^\infty \hat{\tau}_1(k,z)kJ_0(kr)dk \\ \tau_{zz}(r,z) &= \int_0^\infty \hat{\tau}_{zz}(k,z)kJ_0(kr)dk \\ T_p(r,z) &= \int_0^\infty \hat{T}_p(k,z)kJ_0(kr)dk \end{aligned} \quad (84)$$

with $\hat{u}_1 = \frac{\hat{u}_V}{ik}$ and $u_V = \frac{1}{r}\left[\frac{\partial}{\partial r}(ru_r) + \frac{\partial}{\partial\phi}(u_\phi)\right]$, $\hat{\tau}_1 = \frac{\hat{\tau}_{Vz}}{ik}$ and $\tau_{Vz} = \frac{1}{r}\left[\frac{\partial}{\partial r}(r\tau_{rz}) + \frac{\partial}{\partial\phi}(\tau_{\phi z})\right]$.

The displacement stress wavefield vector for a vertical ring source is given by,

$$\left[\ u_1,\ \ u_z,\ \ w_z,\ \ \tau_1,\ \ \tau_{zz},\ \ T_p\ \right]_v^T = \sum_{p=\beta,\alpha_1,\alpha_2} \left(\left[\ \tfrac{1}{ik}\left(-sgn(z-z')U_p^r\right),\ \ -iU_p^z,\ \ -iW_p^z,\ \ \tfrac{1}{ik}\left(iGS_1^p\right),\ \ -sgn(z-z')S_2^p,\ \right] -sgn(z-z')S_3^p \times \frac{r_0}{2} J_0(kr_0) e^{-i\nu_p|z-z'|} \right)^T \tag{85}$$

with variables, $W_\beta^r, W_{\alpha_1}^r, W_{\alpha_2}^r, U_\beta^r, U_{\alpha_1}^r, U_{\alpha_2}^r, W_\beta^z, W_{\alpha_1}^z, W_{\alpha_2}^z, U_\beta^z, U_{\alpha_1}^z, U_{\alpha_2}^z$ defined in (41) and (44). Variables S_1^p, S_2^p, S_3^p with $p = \beta \vee \alpha_1 \vee \alpha_2$ are defined as,

$$\begin{aligned} S_1^\beta &= 2k^2\left[U_\beta^z - \frac{1}{G\nu_\beta}\right], \quad S_1^{\alpha_1} = 2k^2 U_{\alpha_1}^z, \quad S_1^{\alpha_2} = 2k^2 U_{\alpha_2}^z \\ S_2^p &= (H-2G)U_p^r + CW_p^r + H\nu_p U_p^z + C\nu_p W_p^z \\ S_3^p &= C\left[U_p^r + \nu_p U_p^z\right] + M\left[W_p^r + \nu_p W_p^z\right]. \end{aligned} \tag{86}$$

The displacement stress wavefield vector for a radial ring source is given by,

$$\left[\ u_1,\ \ u_z,\ \ w_z,\ \ \tau_1,\ \ \tau_{zz},\ \ T_p\ \right]_r^T = \sum_{i=\beta,\alpha_1,\alpha_2} \left(\left[\ \tfrac{1}{ik}\left(iU_p^r\right),\ \ sgn(z-z')U_p^z,\ \ sgn(z-z')W_p^z,\ \ \tfrac{1}{ik}\left(sgn(z-z')GS_1^p\right),\ \ iS_2^p,\ \ iS_3^p\ \right] \times \frac{r_0}{2} J_1(kr_0) e^{-i\nu_p|z-z'|} \right)^T \tag{87}$$

With variables, $W_\beta^r, W_{\alpha_1}^r, W_{\alpha_2}^r, U_\beta^r, U_{\alpha_1}^r, U_{\alpha_2}^r, W_\beta^z, W_{\alpha_1}^z, W_{\alpha_2}^z, U_\beta^z, U_{\alpha_1}^z, U_{\alpha_2}^z$ defined in (60) and (64). Variables S_1^p, S_2^p, S_3^p with $p = \beta \vee \alpha_1 \vee \alpha_2$ are defined as,

$$\begin{aligned} S_1^p &= U_p^r\nu_p - k^2 U_p^z \\ S_2^p &= (H-2G)U_p^r + CW_p^r - H\nu_p U_p^z - C\nu_p W_p^z \\ S_3^p &= C\left[U_p^r - \nu_p U_p^z\right] + M\left[W_p^r - \nu_p W_p^z\right] \end{aligned} \tag{88}$$

The displacement stress wavefield vector for an explosive ring source is given by,

$$\left[\ u_1,\ \ u_z,\ \ w_z,\ \ \tau_1,\ \ \tau_{zz},\ \ T_p\ \right]_e^T = \sum_{p=\alpha_1,\alpha_2} \left(\left[\ \tfrac{1}{ik}\left(ik^2 U_p^e\right),\ \ -sgn(z-z')\nu_p U_p^e,\ \ -sgn(z-z')\Lambda_p,\ \ \tfrac{1}{ik}sgn(z-z')S_1^p,\ \ iS_2^p,\ \ iS_3^p\ \right] \times \frac{r_0}{2} J_0(kr_0) e^{-i\nu_p|z-z'|} \right)^T \tag{89}$$

with variables, $U_{\alpha_1}^e, U_{\alpha_2}^e$ defined in equation (77). Variables S_1^p, S_2^p, S_3^p with $p = \alpha_1 \vee \alpha_2$ are defined as,

$$S_1^i = 2Gk^2\nu_i U_i^e \tag{90}$$

$$S_2^{\alpha_1} = H\nu_{\alpha_1}^2/kU_{\alpha_1}^e + (H-2G)kU_{\alpha_1}^e + C\Lambda_1\left(\frac{k^2}{\nu_{\alpha_1}} + \nu_{\alpha_1}\right) \quad (91)$$

$$S_2^{\alpha_2} = H\nu_{\alpha_2}^2/kU_{\alpha_2}^e + (H-2G)kU_{\alpha_2}^e + C\Lambda_2\left(\frac{k^2}{\nu_{\alpha_2}} + \nu_{\alpha_2}\right) \quad (92)$$

$$S_3^{\alpha_1} = C\left(k^2 + \nu_{\alpha_1}^2\right)U_{\alpha_1}^e + M\Lambda_1\left(\frac{k^2}{\nu_{\alpha_1}} + \nu_{\alpha_1}\right) \quad (93)$$

$$S_3^{\alpha_2} = C\left(k^2 + \nu_{\alpha_2}^2\right)U_{\alpha_2}^e + M\Lambda_2\left(\frac{k^2}{\nu_{\alpha_2}} + \nu_{\alpha_2}\right). \quad (94)$$

To match the boundary conditions at the borehole wall the w_r and τ_{rr} field components are needed, see equation (1). The radial relative flow component is obtained from the Fourier transformed transformation equation for the fluid expressed in cylindrical coordinates.

$$\hat{T}_p(k,z) = C\left[\hat{u}_1(k,z) + \frac{\partial}{\partial z}\hat{u}_z(k,z)\right] + M\left[\hat{w}_1(k,z) + \frac{\partial}{\partial z}\hat{w}_z(k,z)\right] \quad (95)$$

Therefore,

$$\hat{w}_1(k,z) = -\frac{\partial}{\partial z}\hat{w}_z(k,z) + \frac{1}{M}\left[\hat{T}_p(k,z) - C\left(\hat{u}_1(k,z) + \frac{\partial}{\partial z}\hat{u}_z(k,z)\right)\right]. \quad (96)$$

The radial component can be recovered using equation (103).

The radial stress component is obtained by using the deformation equation for the bulk in cylindrical coordinates.

$$\tau_{rr}(r,z) = H\frac{\partial}{\partial z}u_r(r,z) + [H-2G]u_1(r,z) + C\left[w_1(r,z) + \frac{\partial}{\partial z}w_z(r,z)\right] \quad (97)$$

with $u_1(r,z), w_z(r,z)$ obtained using equation (84) and $w_1(r,z)$ obtained using (56) and (84) and $u_r(r,z)$ obtained using (84) and (103).

MECHANICAL AND ELECTROMAGNETIC WAVES IN HORIZONTALLY LAYERED POROELASTIC MEDIA

We first transform the macroscopic governing equations that control the coupled electromagnetics and acoustics of porous media (Pride and Haartsen, 1995) into a field-vector-formalism that can be solved numerically. The global matrix method (Chin *et al.*, 1984) is employed to solve simultaneously the macroscopic electromagnetic and acoustic-elastic wavefield amplitudes which contribute to current and fluid flow. The current and fluid flow are related by the transport equations through which all electromagnetic and mechanical coupling occurs, i.e., currents generated by the acoustic-elastic wavefields, an electrokinetic phenomenon and fluid flow generated by the electromagnetic field, an osmosis phenomenon. In the global matrix method we propagate a wavefield vector which contains the mechanical stress/displacement and electromagnetic wavefield components

that are continuous through the horizontal boundaries in the layered porous medium (Haartsen and Pride, 1995).

For isotropic media, the first order ordinary differential equations, the equations of state, relating the wavefields at all depths to the medium properties at depth, decompose into two equation sets. The first set describes the $PSVTM$ picture, which is the situation where the compressional and vertical polarized mechanical waves drive currents in the PSV particle motion plane that couple to the electromagnetic wavefield components of the TM mode. The second set describes the $SHTE$ picture where the horizontal polarized rotational waves drive currents in the SH particle motion plane that couples to the electromagnetic wavefield components of the TE mode. In this chapter we compute electroseismograms generated by three mechanical ring sources in the $PSVTM$ polarization picture only.

The effect of a general mechanical ring source in a stratified porous medium is accommodated by specifying a jump in the displacement-stress vector across a horizontal plane, (see Hudson, 1969a,b , and Kennett, 1983). The wavefield components in the displacement-stress vector calculated for a vertical, radial, and explosive ring source, equations (85), (87) and (89) respectively, are the wavefields that are continuous at the horizontal boundaries in the stratified medium for the $PSVTM$ picture (Pride and Haartsen, 1995; Haartsen and Pride, 1995). We define the total displacement-stress-EM wavefield vector as follows,

$$\underline{B} = [u_1, u_2, w_z, \tau_1, \tau_{zz}, T_p, H_2, E_1]^T . \tag{98}$$

At $z = z^{'}$, with z' the source depth only the u_1, τ_{zz} and T_p wavefields jump in the vertical point source representation across a dummy interface. Where a dummy interface denotes a boundary across which none of the medium properties change. The final jump representation across a source plane for a vertical ring source, using equations (85) and (98) reads,

$$\begin{aligned}
\underline{S}(z^{'}) &= \left[\lim_{z\downarrow z^{'}} \underline{B}(z) - \lim_{z\uparrow z^{'}} \underline{B}(z)\right] \\
&= \sum_{p=\beta,\alpha_1,\alpha_2} \Big[-\frac{r_0}{ik^2} U_p^r J_0(kr_0),\ \ 0,\ \ 0,\ \ 0,\ \ -r_0 S_2^p J_0(kr_0), \\
&\quad -r_0 S_3^p J_0(kr_0),\ \ 0,\ \ 0\Big]^T .
\end{aligned} \tag{99}$$

At $z = z^{'}$, with z' the source depth only the u_z, τ_1 and τ_{zz} wavefields jump in the radial ring source representation across a dummy interface. The final jump representation across a source plane for a radial ring source, using equations (87) and (98) reads,

$$\begin{aligned}
\underline{S}(z^{'}) &= \left[\lim_{z\downarrow z^{'}} \underline{B}(z) - \lim_{z\uparrow z^{'}} \underline{B}(z)\right] \\
&= \sum_{p=\beta,\alpha_1,\alpha_2} \Big[0,\ \ r_0 U_p^z J_1(kr_0),\ \ r_0 W_p^z J_1(kr_0),
\end{aligned}$$

$$r_0 \frac{1}{ik} G S_1^p J_1(kr_0), \;\; 0, \;\; 0, \;\; 0, \;\; 0 \Big]^T . \tag{100}$$

At $z = z^{'}$, with z' the source depth only the u_z, τ_1 and τ_{zz} wavefields jump in the radial ring source representation across a dummy interface. The final jump representation across a source plane for an explosive ring source, using equations (89) and (98) reads,

$$\begin{aligned} \underline{S}(z^{'}) &= \left[\lim_{z \downarrow z'} \underline{B}(z) - \lim_{z \uparrow z'} \underline{B}(z) \right] \\ &= \sum_{p=\beta,\alpha_1,\alpha_2} \Big[0, \;\; -r_0 \nu_p U_p^e J_0(kr_0), \;\; -r_0 \Lambda_p J_0(kr_0), \\ &\quad \frac{r_0}{ik} S_1^p J_0(kr_0), \;\; 0, \;\; 0, \;\; 0, \;\; 0 \Big]^T . \end{aligned} \tag{101}$$

Note that the last two electromagnetic wavefield components in equations (99), (100) and (101) are zero since no electromagnetic source is applied.

TRANSFORMATION BACK TO THE SPACE IIME DOMAIN

An inverse Hankel transform is applied to obtain the 3-D spatial dependence of the displacements, stresses, electric, and magnetic fields. The horizontal components of the displacements, stresses, electric, and magnetic fields require additional integration over r and ϕ to obtain, $u_r, u_\phi, \tau_{\phi z}, \tau_{rz}, H_r, H_\phi$ and E_r, E_ϕ due to the definitions of $u_V, u_H, \tau_{Vz}, \tau_{Hz}, H_V, H_H$ and E_V, E_H.

$$u_z(\omega, r, \phi, z) = \int_0^\infty k dk \sum_{n=-N}^{N} \left[J_n(kr) \hat{u}_z(\omega, k, n, z) \right] e^{in\phi} \tag{102}$$

Identical relations exist for w_z, τ_{zz} and T_p.

$$u_r(\omega, r, \phi, z) = \int_0^\infty k dk \sum_{n=-N}^{N} \left[\frac{n}{kr} J_n(kr) \hat{u}_2(\omega, k, n, z) - i J_n'(kr) \hat{u}_1(\omega, k, n, z) \right] e^{in\phi} \tag{103}$$

The horizontal components may be recovered using the following relations:

$$u_\phi(\omega, r, \phi, z) = \int_0^\infty k dk \sum_{n=-N}^{N} \left[\frac{n}{kr} J_n(kr) \hat{u}_1(\omega, k, n, z) + i J_n'(kr) \hat{u}_2(\omega, k, n, z) \right] e^{in\phi} . \tag{104}$$

Identical relations exist for τ_{rz}, $\tau_{\phi z}$ in terms of $\hat{\tau}_1$ and $\hat{\tau}_2$, for E_r, E_ϕ in terms of $\hat{E}_1$ and $\hat{E}_2$ and H_r, H_ϕ in terms of $\hat{H}_1$ and $\hat{H}_2$. The above representations may be regarded as a superposition of cylindrical waves whose order dictates the nature of their azimuthal modulation. At each frequency and angular order the radial contribution is obtained by superposing all horizontal wavenumbers k. This corresponds to including

all propagating waves at the level z within the stratification, from vertically to purely horizontal travelling waves, including the evanescent waves. At any particular distance r the relative contributions of the wavenumbers are imposed by the radial phase functions $J_n(kr)$.

NUMERICAL RESULTS

In this section, we discuss the vertical, radial, and volume injection ring source results in layered media. The final BEM algorithm calls these vertical, radial, and volume injection ring sources in layered medium functions for each source/receiver element combination, including the self interacting elements which are analytically included. The wavefield components, calculated at the receiving elements, that match the boundary conditions across the borehole wall, are calculated by discrete wavenumber integration and each element interaction fills an entry in the square boundary condition matrix. The wavenumber integral becomes computationally more and more expensive with decreasing vertical wavefield propagation, i.e. the interaction between neighboring elements are computationally more expensive than the interaction between further separated elements. Even with all the interacting element symmetries exploited, the BEM solution in layered media is prohibitively computationally expensive. Although numerically feasible on a massive parallel computer, implementing the BEM algorithm on the nCUBE did not have a practical runtime performance.

Therefore, in this section we will the secondary ring source results for three models in the $PSVTM$ wavefield picture only. The first example is a simple surface electroseismic model example (Figure 1). The electroseismic response of the three different ring sources are modelled. In Figures 2, 4 and 6, the mechanical and electroseismograms (TM mode components) are depicted for a volume injection ring source, a vertical and radial ring source. Only the reflection/conversion results are shown, i.e., the direct wavefields are not included. The last two examples show the electroseismic effect in a Vertical Electroseismic Profiling ($VESP$) setting. The seismic ring source is located in the upper halfspace and the recording geophone/antenna are positioned vertically crossing two mechanical/electrical contrasts in the first $VESP$ example (Figure 7) and an additional fluid chemistry contrast in the second $VESP$ example (Figure 11). In Figures 8, 9 and 10 the calculated results are shown for the volume injection ring source, the vertical ring source, and the radial ring source, respectively. Figures 12, 13 and 14 show the additional electroseismic response of the included fluid chemistry contrast within the sand reservoir generated by the three ring sources.

Electroseismics in Surface Geometry

The ring source is positioned 100 m above the contrast and has a 100 Hz center frequency. Fifteen antennas/geophones are positioned symmetrically in a straight horizontal line at both sides of the source, 95 m above the interface. The receiver spacing is 10 m. The medium properties of the two halfspaces and the calculated wave velocities and

bulk conductivities, calculated at source center frequency, are given in Tables I, II and III. All plots in Figures 2, 4 and 6 are seismogram scaled. When a volume injection ring source is set off, only P waves are generated in an isotropic poroelastic medium while the vertical and radial ring sources generate P as well as SV waves. The mechanical displacement seismograms (u_z and u_x components) in Figures 4 and 6 show clearly the difference in amplitude variablity versus offset to be expected for vertical and radial ring sources. For example, the u_z component in the PP reflection is maximum at zero offset reflection for a vertical ring source, while the same wavefield component is minimum at zero offset reflection for a radial ring source.

The converted TM wavefield components show up at all antennas at approximately half the two-way P wave traveltime for normal incidence reflection. The hyperbolas arriving at later time in the E_x and H_y electroseismograms appear at the same traveltime as the PP reflection, PSV conversion and $SVSV$ reflection, SVP conversion for the vertical and radial ring sources only. The electric fields travelling with compressional wavespeed through a homogeneous porous medium are caused by a charge separation generated by pressure gradients inside the seismic pulse. The magnetic fields travelling with rotational wavespeed through homogeneous porous medium are induced by current sheets generated by the divergence free grain accelerations.

The vertical and radial ring sources generate radiating EM wavefields. These fields show up in the electroseismograms (Figures 4 and 6) at approximately zero traveltime. The electroseismograms are slightly shifted in time to avoid signal wrapping in time, which will be introduced by the convolution of the impulse response with a non-causal Ricker wavelet (Hosken, 1988). Physically, a vertical and radial ring source induce a vertical and radial streaming current, respectively, at a hypothetical source plane, due to a mechanically driven vertical and radial relative flow. The electromagnetic fields associated with these mechanically induced streaming currents at the source plane need to be balanced by electromagnetic fields that make the E_x and H_y field component entries in the vertical and radial jump representations across the source plane vanish, see equations (99) and (100), respectively. Due to symmetry properties, the volume injection ring source doesn't radiate EM fields away from the mechanical source. In Figures 3 and 5 the expected radiation pattern for a vertical and radial ring source above a contrast is outlined. The amplitude behavior of the reflected electromagnetic signal is depicted for a hypothetical perfect reflector case, using the method of images. The horizontal component of the reflected electromagnetic field is zero right at the center of the ring sources and increases with horizontal distance. This amplitude behavior can be identified in the electroseismograms in Figures 4 and 6 and the cartoons in Figures 3 and 5. The length of the arrows in Figures 3 and 5 are an indication of the the absolute field amplitudes. The reflected EM wavefields generated by the radial ring source are much smaller than the fields generated by a vertical ring source.

The electroseismic conversion of an incoming SV wave generated by the vertical and radial ring sources is insignificant to the pressure gradient, P wave induced converted electromagnetic signals. The SV to EM conversion is not discernible at the the used

electroseismogram scaling in Figures 4 and 6. The importance of a dynamic vertical pressure gradient imbalance in the conversion to electromagnetic signals is evident when we compare the volume injection and vertical ring source results with the radial ring source result. The P wave conversion into electromagnetic signal is orders of magnitude smaller in the radial ring source synthetics, since its P wave radiation pattern points mainly to the horizontal direction parallel to the contrast, as opposed to the volume injection and vertical ring source radiation pattern that point their P wave energy mainly towards the contrast.

Electroseismograms in VESP Geometry

In the $VESP$ geometry the antennas are positioned close to the target of interest and therefore larger converted electromagnetic signals can be recorded before they become too attenuated with travelled distance. With the $VESP$ technique, the electroseismic method can be extended to targets (electrical and/or mechanical contrasts) at greater depths. The first $VESP$ example is a sandwiched reservoir sand in between two low permeability halfspaces with smaller porosity. The first receiver/antenna is positioned at 20 m horizontal offset and a depth of 40 m. The receiver/antenna spacing is 5 m. The model is depicted in Figure 7. The complete set of medium properties and the at source center frequency calculated wavefield velocities and bulk conductivities are given in Tables I, II and III. In Figures 8, 9 and 10, the numerically calculated $VESP$'s are shown for a volume injection source, a vertical, and radial ring source. The top plot shows the mechanical displacement response, the center and bottom plots show the E_x and H_y TM medium components, respectively.

The converted TM wavefield components show up at all receiving antennas at approximately the same time. These events can be recognized as the straight vertical lines in the figures. All later arrivals in the E_x $VESP$ are the electric fields within the seismic pulse that travel with the compressional wavespeed. The later arrivals in the H_y $VESP$ are the magnetic fields within the seismic pulse that travel with the rotational wavespeed. When we compare the electroseismograms generated by a vertical and radial ring source, we notice the very strong SV and SV induced signals in the radial ring source seismogram and electroseismograms. The vertical ring source seismogram shows strong P wave conversions into TM signal. The conversion from SV into TM signal is very weak for the shear waves generated by the vertical ring source. The radial ring source on the other hand shows strong SV to electromagnetic wave conversions. The SV wave converted signals are in this case larger in amplitude than the P wave converted signals.

The last numerical example has an additional electrical contrast added to the previous model (Figure 11). The 100 m thick "reservoir sand" is divided into two sands with identical mechanical properties saturated with two fluids of different salinity. In Figures 12, 13 and 14 the calculated $VESP$'s for a volume injection ring source, a vertical and a radial ring source are shown, respectively. The mechanical response is identical to the previous calculations without the electrical fluid contrast (Figures 8, 9 and 10). But the

TM mode component $VESP$'s show an additional electroseismic conversion generated at the electrical contrast.

CONCLUSIONS AND DISCUSSION

The Biot-Rosenbaum model is extended by including the effect of a heterogeneous formation surrounding the borehole and by including the conversions of mechanical into electromagnetic waves at the mechanical and/or electrical contrasts in the poroelastic formation. The method is formulated as a boundary element technique where the poroelastic mechanical wavefield components to be matched across the borehole wall are calculated by the discrete wavenumber method, integrating the dynamic poroelastic Green's function wavefield solutions. The coupled electromagnetic and acoustic wavefields in layered media are included by employing the global matrix technique.

The singular properties of the stress field for the dynamic Green's functions with a force applied on the solid phase and the singular property of the displacement for the dynamic Green's function with a force applied on the fluid phase, when source and receiving element coincide, are determined analytically by integration of the derived static Green's functions over a half spherical surface.

Four secondary ring sources are introduced: a volume injection ring source (generating wavefields diffracted into the fluid), a vertical and radial ring source acting on the elastic frame, and a volume injection ring source acting on the pore fluid. The last three sources give rise to the wavefields radiated into the poroelastic formation.

The developed BEM algorithm needs to be optimized to decrease its runtime on the nCUBE to allow full waveform modelling of seismic and converted electromagnetic waves in a borehole embedded in a layered porous medium. The Stoneley waves and converted electromagnetic signals both contain information about permeability. The converted electromagnetic signals are also sensitive to fluid chemistry contrasts (i.e. oil-water contact) in a homogeneous reservoir. The study of these effects on the full waveforms awaits the optimization of the developed algorithm.

In this paper, three mechanical source jump representations for the three ring sources in the poroelastic formation are derived. These jump conditions are included in the global matrix technique and constitute the kernel program functions of the BEM algorithm. The numerical results show that the vertical and radial ring sources generate radiating electromagnetic fields. The induced step in electrical streaming current imposes a jump in electromagnetic fields to accommodate for the predefined zero magnetic and electric field components (since no electromagnetic source is applied) in the vertical and radial ring source jump representations across the source plane.

The conversion to electromagnetic disturbances is found to be mainly due to pressure gradients generated by the P waves across the contrasts for the vertical and volume injection ring source. Even though rotational waves generated by the vertical ring source induce larger streaming currents, they do not necessarily create larger current imbalances across the interface and therefore no larger converted electromagnetic distur-

bances, whereas in the radial ring source case, the SV wave induced current imbalances across the contrasts account for the main conversions to electromagnetic disturbances. This illustrates the magnitude dependence of the electroseismic conversions from SV waves, on the SV radiation pattern orientation with respect to the interface.

REFERENCES

Biot, M. A., Theory of propagation of elastic waves in a fluid saturated porous solid. I. Low frequency range. II. Higher frequency range, *J. Acoust. Soc. Am., 28,* 168–191, 1956.

Bouchon, M., Propagation of elastic waves in cylindrical bore containing a fluid, *J. Applied Physics, 23,* 977–1005, 1952.

Bouchon, M., A numerical simulation of the acoustic and elastic wave fields radiated by a source in a fluid-filled borehole embedded in a layered medium, *Geophysics, 58,* 475–481, 1993.

Bouchon, M. and K. Aki, Discrete-wavenumber representation of seismic source wavefields, *Bull. Seis. Soc. Am., 67,* 259–277, 1977.

Brebia, C. and J. Dominguez, *Boundary Elements: An Introductory Course,* McGraw-Hill Inc., New York, 1989.

Burns, D. and C. Cheng, Determination of in-situ permeability from tube wave velocity and attenuation, in *27th Symposium, Paper KK,* Society of Professional Well Log Analysts, Transactions, 1986.

Cheng, N., Borehole wave propagation in isotropic and anisotropic media: Three-dimensional finite difference approach, Ph.D. Thesis, Massachusetts Institute of Technology, Cambridge, MA, 1994.

Chin, R. C. Y., G. W. Hedstrom, and L. Thigpen, Matrix methods in synthetic seismograms, *Geophys. J. Roy. astron. Soc. 77,* 483–502, 1984.

de la Cruz, V. and T. J. T. Spanos, Seismic boundary conditions for porous media, *J. Geophys. Res., 94,* 3025–3029, 1989.

Deresiewicz, H. and R. Skalak, On the uniqueness in dynamic poroelasticity, *Bull. Seis. Soc. Am.,* pp. 783–788, 1963.

Dong, W., Elastic wave radiation from borehole seismic sources in anisotropic media, Ph.D. Thesis, Massachusetts Institute of Technology, Cambridge, MA, 1993.

Haartsen, M., Coupled electromagnetic and acoustic wavefield modelling in poroelastic media and its applications in geophysical exploration, Ph.D. Thesis, Massachusetts Institute of Technology, Cambridge, MA, 1995.

Haartsen, M. and S. Pride, Modeling of coupled electroseismic waves from point sources in layered media (to be submitted), *J. Geophys. Res.,* 1995.

Hornby, B.E., D.L Johnston, K. W. and R. Plumb, Fracture evaluation using reflected Stoneley wave arrivals, *Geophysics, 54,* 1274–1288, 1989.

Hosken, J., Ricker wavelets in their various guises, *First Break, 6,* 25–33, 1988.

Hsui, A. and M. N. Toksoz, Application of an acoustic model to determine in-situ permeability, *J. Acoust. Soc. Am., 79,* 2055–2059, 1986.

Hudson, J. A., A quantitative evaluation of seismic signals at teleseismic distances i-radiation from a point source, *Geophys. J. Roy. Astron. Soc., 18,* 133–249, 1969a.

Hudson, J. A., A quantitative evaluation of seismic signals at teleseismic distances ii-body waves and surface waves from an extended source, *Geophys. J. Roy. Astron. Soc., 18,* 353–370, 1969.

Kennett, B. L. N. , *Seismic wave propagation in stratified media,* Cambridge University Press, 1983.

Kupradze, V. D., *Dynamical Problems in Elasticity,* Vol. III, North-Holland, Amsterdam, 1963.

Love, A. E. H., *A Treatise on the Mathematical Theory of Elasticity* (4th edition), Dover, New York, N.Y., 1944.

Lovera, O. M., Boundary conditions for a fluid-saturated porous solid, *Geophysics, 52,* 174–178, 1987.

Paillet, F.L. and X. Tang, Theoretical models relating acoustic tube wave attenuation to fracture permeability—reconciling model results with field data, in *30th Symposium, Paper FF,* Society of Professional Well Log Analysts, Transactions, 1989.

Pride, S. and M. Haartsen, Electroseismic waves in poroelastic media (to be submitted), *J. Acoust. Soc. Am.,* 1995.

Rosenbaum, J., Synthetic microseismogram: logging in porous formations, *Geophysics, 39,* 14–32, 1974.

Schmitt, D., Acoustic multipole logging in transversely isotropic poroelastic formations, *J. Acoust. Soc. Am., 86,* 2397–2421, 1989.

Schmitt, D.P. and G. Bonnet, Full waveform synthetic acoustic logs in radially semi-infinite saturated porous media, *Geophysics, 53,* 807–823, 1988.

Stephen, R.A. and C. Cheng, Finite difference synthetic acoustic logs, *Geophysics, 50,* 1588–1608, 1985.

Tang, X., Acoustic logging in fractured and porous formations, Ph.D. Thesis, Massachusetts Institute of Technology, Cambridge, MA, 1990.

Tang, X.M. and M. Toksöz, Dynamic permeability and borehole Stoneley waves: A simplified Biot-Rosenbaum model, *J. Acoust. Soc. Am., 90,* 1632–1646, 1991.

Watson, G. N., *A Treatise on the Theory of Bessel Functions* (2nd edition), Cambridge University Press, 1966.

White, J., *Underground Sound,* Elsevier Science Pub. Co., 1983.

Williams, D., J. Zemanek, F. Angona, C. Denis, and R. Caldwell, The long spaced acoustic logging tool, in *25th Symposium, Paper T,* Society of Professional Well Log Analysts, Transactions, 1984.

Winkler, K.W. and D. Johnson, Permeability and borehole Stoneley waves: Comparison between experiment and theory, *Geophysics, 54,* 66–75, 1989.

TABLE I. The medium properties in the layers used in the numerical calculations.

Property	Top and bottom halfspaces	Salinity I layer	Salinity II layer	Salinity III halfspace
porosities ($\phi[\%]$)	15	30	30	30
dc permeability ($k[m^2]$)	10^{-14}	10^{-12}	10^{-12}	10^{-12}
bulk modulus solid ($k_s[Pa]$)	3.0×10^{10}	1.0×10^{10}	1.0×10^{10}	1.0×10^{10}
bulk modulus fluid ($k_f[Pa]$)	2.2×10^9	2.2×10^9	2.2×10^9	2.2×10^9
frame bulk modulus ($k_{fr}[Pa]$)	8.0×10^9	3.0×10^9	3.0×10^9	3.0×10^9
frame shear modulus ($g_{fr}[Pa]$)	9.0×10^9	8.5×10^9	8.5×10^9	8.5×10^9
fluid viscosity ($\eta[Pas]$)	1.0×10^{-3}	1.0×10^{-3}	1.0×10^{-3}	1.0×10^{-3}
density solid ($\rho_s[Kg/m^3]$)	2.7×10^3	2.7×10^3	2.7×10^3	2.7×10^3
density fluid ($\rho_f[Kg/m^3]$)	1.0×10^3	1.0×10^3	1.0×10^3	1.0×10^3
salinity ($C[mol/l]$)	1.0×10^{-3}	$1.0\ 10^{-2}$	1.0×10^{-1}	1.0
temperature ($T[K]$)	298	298	298	298
permittivity (κ_f)	80	80	80	80
permittivity (κ_s)	4	4	4	4
tortuosity (α_∞)	3	3	3	3

TABLE IIa. The calculated (at center frequency) wavefield velocities and bulk conductivities in the surface seismic and VESP geometry models.

Properties	Upper and lower halfspace	Salinity I layer
fast wave velocity$[m/s]$	(3154.97, -0.00011)	(2502.21, -0.0524)
slow wave velocity$[m/s]$	(5.52, -5.28)	(40.54, -38.17)
shear wave$[m/s]$	(1768.85, -0.00248)	(1648.32, -0.258)
TM wave velocity$[m/s]$	(827466.0/-792166.0)	(192248.0/-184061.0)
conductivity ($\sigma[S/m]$)	0.000416	0.0771

TABLE IIb. The calculated (at center frequency) wavefield velocities and bulk conductivities in the surface seismic and VESP geometry models.

Properties	Salinity III halfspace
fast wave velocity$[m/s]$	(2502.21, -0.0524)
slow wave velocity$[m/s]$	(40.54, -38.17)
shear wave$[m/s]$	(1648.32, -0.258)
TM wave velocity$[m/s]$	(19238.2, -18419.1)
conductivity ($\sigma[S/m]$)	0.77

Appendix A. DYNAMIC AND STATIC GREEN'S FUNCTIONS IN POROELASTIC MEDIA

Displacement Green's Function with Source on Frame

To evaluate the element surface integrals, the following poroelastic Green's functions are used. The detailed derivation of the dynamic Green's functions is outlined in (Haartsen, 1995, chapter 5).

$$\underline{\underline{G}}^u_s = g^u \underline{\underline{I}} + \left[G - \frac{1}{M}(HM - C^2)\right] \nabla\nabla\phi - \left[-2\omega^2\rho_f C + M\omega^2\frac{\rho_f^2}{\rho_E} + \frac{C^2}{M}\omega^2\rho_E\right] \nabla\nabla\phi^* \quad \text{(A-1)}$$

where the superscript u denotes the Green's function to be a displacement Green's function and subscript s denotes a point force applied to the solid matrix. With,

$$\phi = B(us)g_\beta + A_1(us)g_{\alpha 1} + A_2(us)g_{\alpha 2} = B(us)\frac{e^{ik_\beta R}}{4\pi R} + A_1(us)\frac{e^{ik_{\alpha 1} R}}{4\pi R} + A_2(us)\frac{e^{ik_{\alpha 2} R}}{4\pi R}. \quad \text{(A-2)}$$

With the introduced variables $B(us), A_1(us), A_2(us)$, where (us) denotes scalar Green's function amplitudes belonging to the displacement Green's function with a source applied on the solid frame defined as,

$$\begin{aligned}
B(us) &= \frac{1}{G\left[HM - C^2\right]} \frac{-k_\beta^2 M + \omega^2\rho_E}{\left(k_\beta^2 - k_{\alpha 1}^2\right)\left(k_\beta^2 - k_{\alpha 2}^2\right)} \\
A_1(us) &= \frac{1}{G\left[HM - C^2\right]} \frac{-k_{\alpha 1}^2 M + \omega^2\rho_E}{\left(k_{\alpha 1}^2 - k_\beta^2\right)\left(k_{\alpha 1}^2 - k_{\alpha 2}^2\right)} \\
A_2(us) &= \frac{1}{G\left[HM - C^2\right]} \frac{-k_{\alpha 2}^2 M + \omega^2\rho_E}{\left(k_{\alpha 2}^2 - k_\beta^2\right)\left(k_{\alpha 2}^2 - k_{\alpha 1}^2\right)}
\end{aligned} \quad \text{(A-3)}$$

where ϕ^* is defined as,

$$\phi^* = B^*(us)g_\beta + A_1^*(us)g_{\alpha 1} + A_2^*(us)g_{\alpha 2}. \quad \text{(A-4)}$$

With the variables $B^*(us), A_1^*(us), A_2^*(us)$ (variables $B(us), A_1(us), A_2(us)$ divided by Ξ) defined as,

$$B^*(us) = \frac{B(us)}{\omega^2\rho_E - Mk_\beta^2}, \quad A_1^*(us) = \frac{A_1(us)}{\omega^2\rho_E - Mk_{\alpha 1}^2}, \quad A_2^*(us) = \frac{A_2(us)}{\omega^2\rho_E - Mk_{\alpha 2}^2}. \quad \text{(A-5)}$$

With the displacement scalar shear Green's function,

$$g^u(\mathbf{x}, \mathbf{x}') = \frac{e^{ik_0 R}}{4\pi G R} \quad \text{(A-6)}$$

where $R = \sqrt{(x - x')^2 + (y - y')^2 + (z - z')^2}$ is the distance from the source to the receiver and $k_0 = \omega/\sqrt{G/(\rho_B - \frac{\rho_f^2}{\rho_E})}$ is the wavenumber.

Relative Flow Green's Function with Source on Frame

$$\begin{aligned}\underline{\underline{G}}_s^w &= g^w \underline{\underline{I}} + \left[\frac{1}{C}(HM - C^2) - G\frac{\rho_E}{\rho_f}\right]\nabla\nabla\Phi \\ &- \left[\frac{HM}{C}\omega^2\rho_f + C\omega^2\frac{\rho_B\rho_E}{\rho_f} - H\omega^2\rho_E - M\omega^2\rho_B\right]\nabla\nabla\Phi^* \qquad \text{(A-7)}\end{aligned}$$

where the superscript w denotes the Greens's function to be a relative flow Green's function and the subscript s denotes the point force applied to the solid matrix. With,

$$\Phi = B(ws)g_\beta + A_1(ws)g_{\alpha 1} + A_2(ws)g_{\alpha 2} = B(ws)\frac{e^{ik_\beta R}}{4\pi R} + A_1(ws)\frac{e^{ik_{\alpha 1}R}}{4\pi R} + A_2(ws)\frac{e^{ik_{\alpha 2}R}}{4\pi R}. \text{(A-8)}$$

With the introduced variables $B(ws), A_1(ws), A_2(ws)$, where (ws) denotes scalar Green's function amplitudes belonging to the relative flow Green's function with a source applied on the solid frame defined as,

$$\begin{aligned}B(ws) &= \frac{1}{G\left[HM - C^2\right]\frac{\rho_E}{\rho_f}}\frac{-k_\beta^2 C + \omega^2\rho_f}{\left(k_\beta^2 - k_{\alpha 1}^2\right)\left(k_\beta^2 - k_{\alpha 2}^2\right)} \\ A_1(ws) &= \frac{1}{G\left[HM - C^2\right]\frac{\rho_E}{\rho_f}}\frac{-k_{\alpha 1}^2 C + \omega^2\rho_f}{\left(k_{\alpha 1}^2 - k_\beta^2\right)\left(k_{\alpha 1}^2 - k_{\alpha 2}^2\right)} \\ A_2(ws) &= \frac{1}{G\left[HM - C^2\right]\frac{\rho_E}{\rho_f}}\frac{-k_{\alpha 2}^2 C + \omega^2\rho_f}{\left(k_{\alpha 2}^2 - k_\beta^2\right)\left(k_{\alpha 2}^2 - k_{\alpha 1}^2\right)} \qquad \text{(A-9)}\end{aligned}$$

where Φ^* is defined as,

$$\Phi^* = B^*(ws)g_\beta + A_1^*(ws)g_{\alpha 1} + A_2^*(ws)g_{\alpha 2}. \qquad \text{(A-10)}$$

With the variables $B^*(ws), A_1^*(ws), A_2^*(ws)$ (variables $B(ws), A_1(ws), A_2(ws)$, divided by ξ) defined as,

$$B^*(ws) = \frac{B(ws)}{\omega^2\rho_f - Ck_\beta^2}, \quad A_1^*(ws) = \frac{A_1(ws)}{\omega^2\rho_f - Ck_{\alpha 1}^2}, \quad A_2^*(ws) = \frac{A_2(ws)}{\omega^2\rho_f - Ck_{\alpha 2}^2}. \text{(A-11)}$$

The relative flow scalar shear Green's function is given by,

$$g^w(\mathbf{x}, \mathbf{x}') = -\frac{\rho_f}{\rho_E}\frac{e^{ik_0 R}}{4\pi G R} \qquad \text{(A-12)}$$

where $R = \sqrt{(x - x')^2 + (y - y')^2 + (z - z')^2}$ is the distance from the source to the receiver and $k_0 = \omega/\sqrt{G/(\rho_B - \frac{\rho_f^2}{\rho_E})}$ is the wavenumber.

Displacement Green's Function with Source on Fluid

$$\begin{aligned}\underline{\underline{G}}_f^u &= \nabla \cdot \underline{\underline{G}}_s^w \\ &= \frac{1}{C}\left[C^2 - HM + GC\frac{\rho_E}{\rho_f}\right]\nabla\Pi + \left[\frac{HM}{C}\omega^2\rho_f + C\omega^2\frac{\rho_B\rho_E}{\rho_f} - H\omega^2\rho_E\right. \\ &\quad \left. -M\omega^2\rho_B\right]\nabla\Pi^* \qquad \text{(A-13)}\end{aligned}$$

where Π and Π^* are defined as,

$$\begin{aligned}\Pi &= -\left[A_1(ws)k_{\alpha_1}^2 g_{\alpha_1} + A_2(ws)k_{\alpha_2}^2 g_{\alpha_2}\right] = -A_1(ws)k_{\alpha_1}^2\frac{e^{ik_{\alpha_1}R}}{4\pi R} \\ &\quad -A_2(ws)k_{\alpha_2}^2\frac{e^{ik_{\alpha_2}R}}{4\pi R} \qquad \text{(A-14)} \\ \Pi^* &= -\left[A_1^*(ws)k_{\alpha_1}^2 g_{\alpha_1} + A_2^*(ws)k_{\alpha_2}^2 g_{\alpha_2}\right] = -A_1^*(ws)k_{\alpha_1}^2\frac{e^{ik_{\alpha_1}R}}{4\pi R} \\ &\quad -A_2^*(ws)k_{\alpha_2}^2\frac{e^{ik_{\alpha_2}R}}{4\pi R}. \qquad \text{(A-15)}\end{aligned}$$

The variables $A_1(ws), A_2(ws)$ and $A_1^*(ws), A_2^*(ws)$ are defined in equations (A-8) and (A-10), respectively.

Relative Flow Green's Function with Source on Fluid

$$\underline{\underline{G}}_f^w = \nabla\Pi^*, \quad \Pi^* = \Lambda_1 g_{\alpha_1} + \Lambda_2 g_{\alpha_2} \qquad \text{(A-16)}$$

where,

$$\begin{aligned}\Lambda_1 &= \left[HG\omega^2\rho_E\left(k_{\alpha_1}^2k_\beta^2 - k_{\alpha_1}^4\right) + \omega^4\rho_E\rho_B G\left(k_{\alpha_1}^2 - k_\beta^2\right)\right]A_1^*(wf) \\ \Lambda_2 &= \left[HG\omega^2\rho_E\left(k_{\alpha_2}^2k_\beta^2 - k_{\alpha_2}^4\right) + \omega^4\rho_E\rho_B G\left(k_{\alpha_2}^2 - k_\beta^2\right)\right]A_2^*(wf) \\ A_1^*(wf) &= \frac{A_1(wf)}{\left(\omega^2\rho_B - k_{\alpha_1}^2H\right)\left(\omega^2\rho_B - k_{\alpha_1}^2G\right)}, \\ A_2^*(wf) &= \frac{A_2(wf)}{\left(\omega^2\rho_B - k_{\alpha_1}^2H\right)\left(\omega^2\rho_B - k_{\alpha_1}^2G\right)}. \qquad \text{(A-17)}\end{aligned}$$

With the introduced variabels $A_1(wf), A_2(wf)$, where (wf) denotes scalar Green's function amplitudes belonging to the relative flow Green's function with a source applied on the fluid phase defined as,

$$\begin{aligned}A_1(wf) &= \frac{1}{G\omega^2\rho_E\left[HM - C^2\right]}\frac{\left(\omega^2\rho_B - k_{\alpha_1}^2H\right)\left(\omega^2\rho_B - k_{\alpha_1}^2G\right)}{\left(k_{\alpha_1}^2 - k_\beta^2\right)\left(k_{\alpha_1}^2 - k_{\alpha_2}^2\right)} \\ A_2(wf) &= \frac{1}{G\omega^2\rho_E\left[HM - C^2\right]}\frac{\left(\omega^2\rho_B - k_{\alpha_2}^2H\right)\left(\omega^2\rho_B - k_{\alpha_2}^2G\right)}{\left(k_{\alpha_2}^2 - k_\beta^2\right)\left(k_{\alpha_2}^2 - k_{\alpha_1}^2\right)}. \qquad \text{(A-18)}\end{aligned}$$

Static Green's Functions in Poroelastic Media

Static Displacement Green's Function

To determine the singular behavior of the dynamic Green's function when a field point approaches the source point, the static case must be considered. This regularizes the surface integrals of the dynamic Green's function (Kupradze, 1963). When ω is set to zero, a static Green's function is obtained. To obtain the g^u and ϕ equations in the static limit we have to be solve,

$$G\nabla_t^2 g^u + G\frac{\partial^2}{\partial z^2} g^u = -\delta\left(\mathbf{x}-\mathbf{x}'\right) \tag{A-19}$$

$$\frac{G}{M}\left[HM-C^2\right]\left[\nabla_t^2+\frac{\partial^2}{\partial z^2}\right]^2 \phi = -\delta\left(\mathbf{x}-\mathbf{x}'\right). \tag{A-20}$$

The solution of equation (A-19) is

$$g^u = \frac{1}{4\pi G}\frac{1}{R}. \tag{A-21}$$

The solution of equation (A-20), using Poisson's equation $\nabla^2\frac{1}{4\pi R} = -\delta\left(\mathbf{x}-\mathbf{x}'\right)$ and the identity $\nabla^2 R = \frac{2}{R}$ is,

$$\phi = \frac{M}{8\pi G\left[HM-C^2\right]}R \tag{A-22}$$

With $R=\sqrt{(x-x')^2+(y-y')^2+(z-z')^2}$. Substituting ϕ and g into equation (A-1) in the static limit yields,

$$\underline{\underline{G}} = \frac{1}{4\pi G}\frac{1}{R}\underline{\underline{I}} - \frac{\frac{1}{M}\left[HM-C^2-GM\right]}{8\pi\frac{G}{M}\left[HM-C^2\right]}\nabla\nabla R. \tag{A-23}$$

Taking the isotropic elastic limit, physically meaning the collapse of the pore space ($\phi \rightarrow 0$), of equation (A-23) gives,

$$\underline{\underline{G}} = \frac{1}{4\pi\mu}\frac{1}{R}\underline{\underline{I}} - \frac{\lambda+\mu}{8\pi\mu(\lambda+2\mu)}\nabla\nabla R \tag{A-24}$$

which is the isotropic elastic static Green's function (Love, 1944).

Static Relative Flow Green's Function

To obtain the g^w and Φ equations in the static limit we have to solve,

$$-G\frac{\rho_E}{\rho_f}\nabla_t^2 g^w - G\frac{\rho_E}{\rho_f}\frac{\partial^2}{\partial z^2}g^w = -\delta\left(\mathbf{x}-\mathbf{x}^{'}\right) \tag{A-25}$$

$$\frac{G}{C}\frac{\rho_E}{\rho_f}\left[HM-C^2\right]\left[\nabla_t^2+\frac{\partial^2}{\partial z^2}\right]^2\Phi = -\delta\left(\mathbf{x}-\mathbf{x}^{'}\right). \tag{A-26}$$

The solution of equation (A-25) is

$$g^w = -\frac{1}{4\pi G}\frac{1}{R\frac{\rho_E}{\rho_f}}. \tag{A-27}$$

The solution of equation (A-26), using Poisson's equation $\nabla^2\frac{1}{4\pi R} = -\delta\left(\mathbf{x}-\mathbf{x}^{'}\right)$ and the identity $\nabla^2 R = \frac{2}{R}$ is,

$$\Phi = \frac{C\rho_f}{8\pi G\rho_E\left[HM-C^2\right]}R \tag{A-28}$$

with $R = \sqrt{(x-x')^2+(y-y')^2+(z-z')^2}$. Substituting ϕ and g into equation (A-7) in the static limit yields,

$$\underline{\underline{G}} = -\frac{1}{4\pi G}\frac{1}{\frac{\rho_E}{\rho_f}R}\underline{\underline{I}} + \frac{\frac{1}{C}\left[HM-C^2-GC\frac{\rho_E}{\rho_f}\right]}{8\pi\frac{G}{C}\frac{\rho_E}{\rho_f}\left[HM-C^2\right]}\nabla\nabla R. \tag{A-29}$$

In the static limit, $\omega \rightarrow 0$, the effective fluid density reduces to the fluid density in the pore space, $\rho_E \rightarrow \rho_f$.

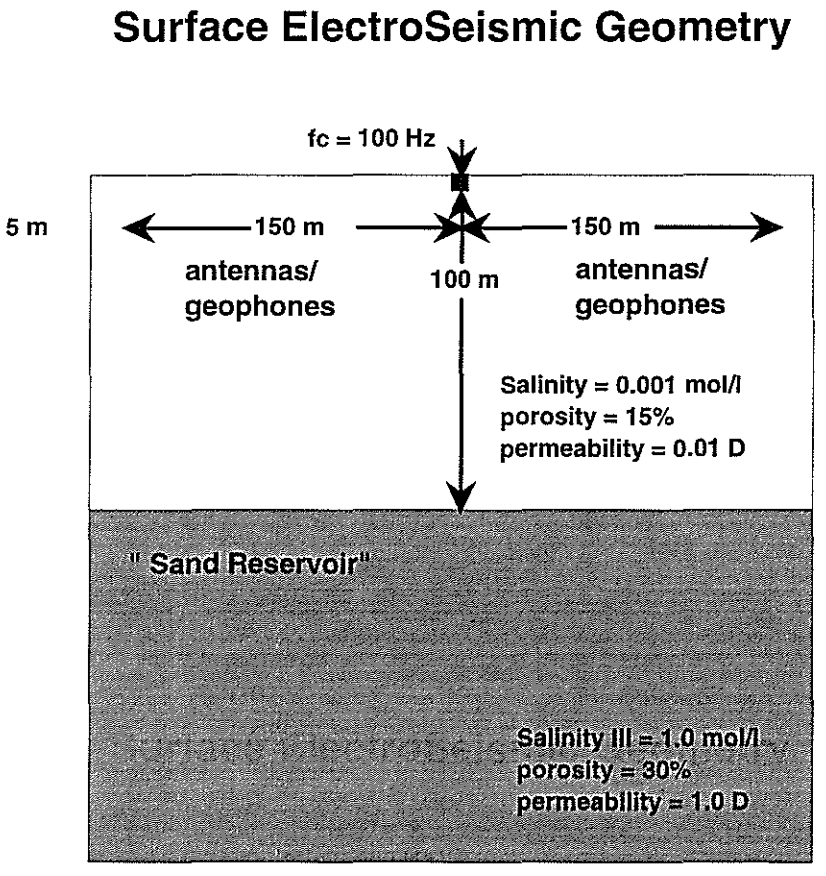

Figure 1: An explosive and vertical point source 100 m above an interface in a surface electroseismic geometry setting.

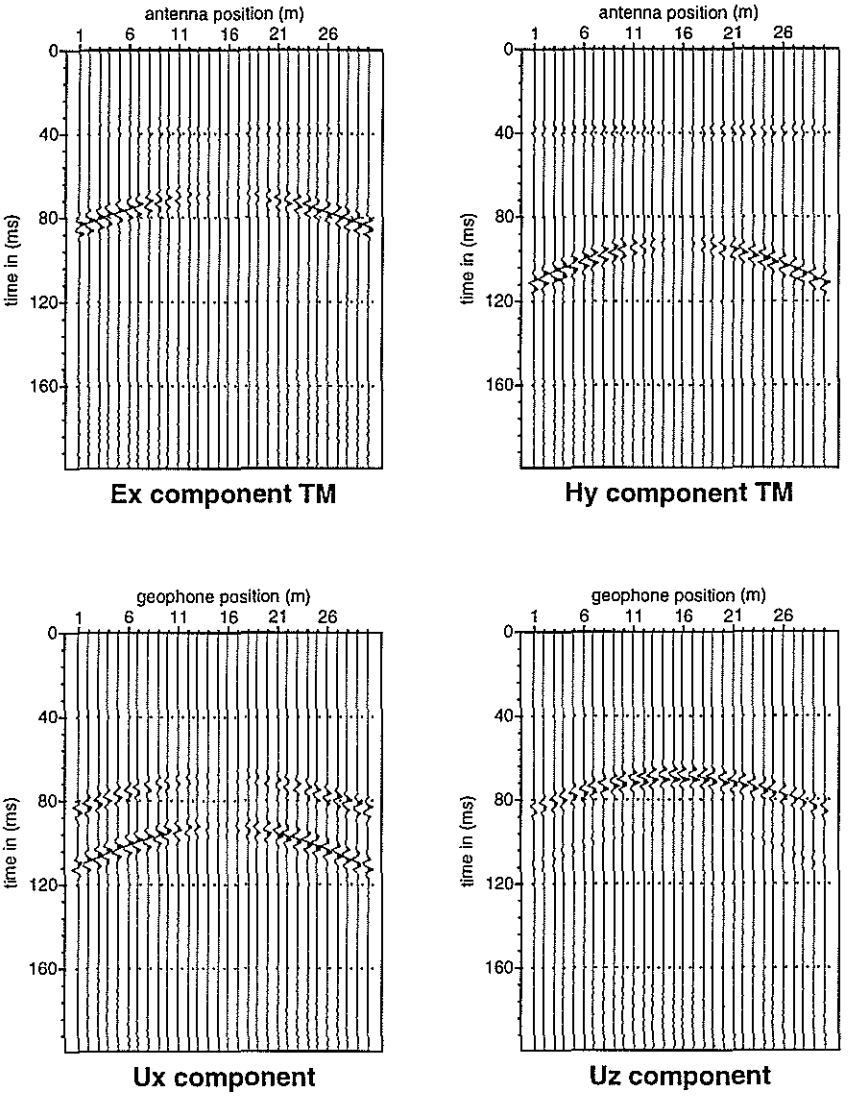

Figure 2: The mechanical displacement component seismograms and the TM mode component electroseismograms, without direct waves, calculated for an explove ring source above a one interface model.

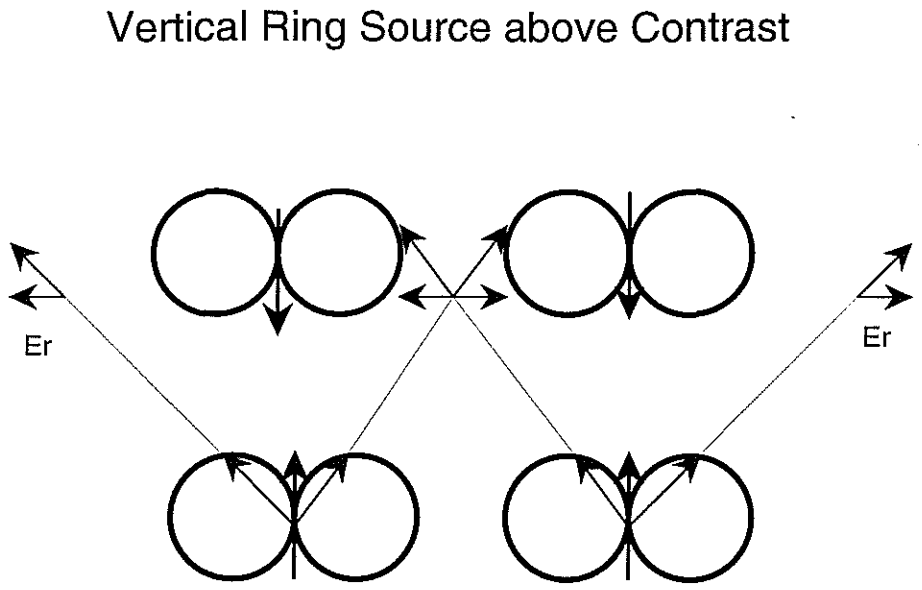

Figure 3: Vertical ring source above a contrast.

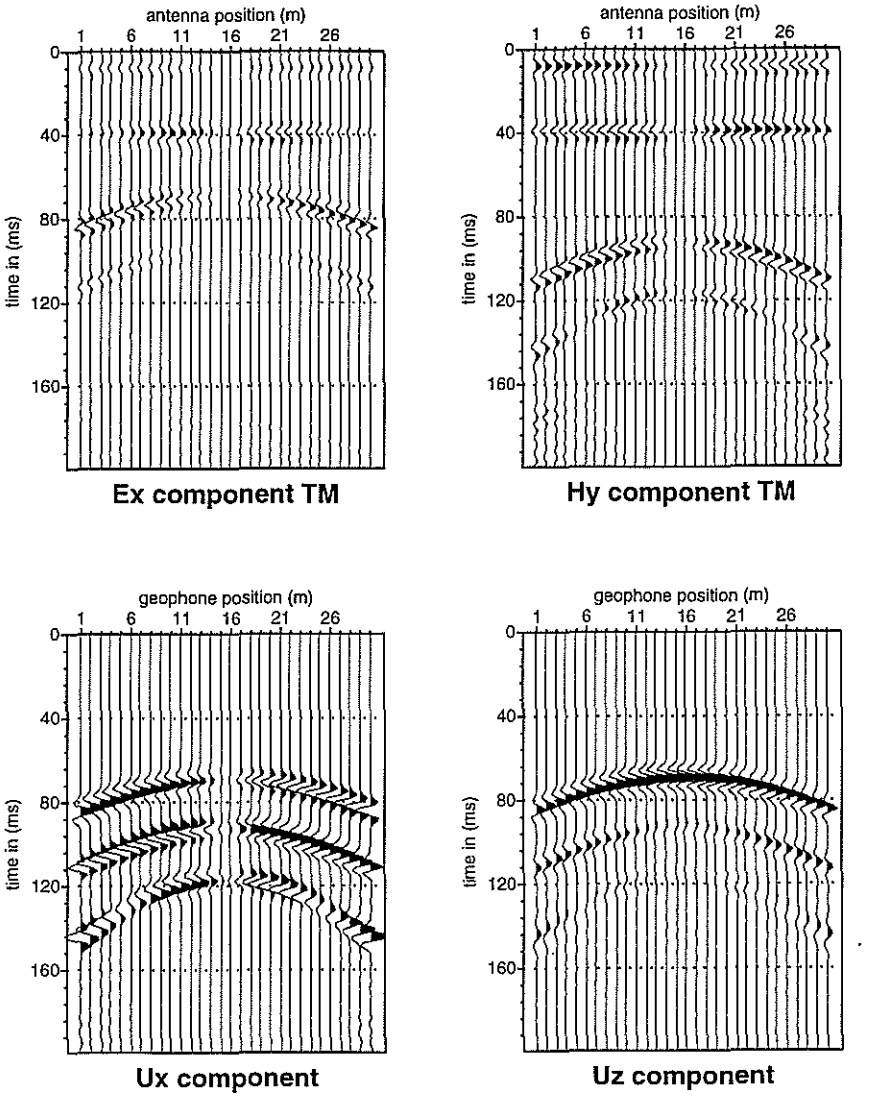

Figure 4: The mechanical displacement component seismograms and the TM mode component electroseismograms, without direct waves, calculated for a vertical ring source above a one interface model.

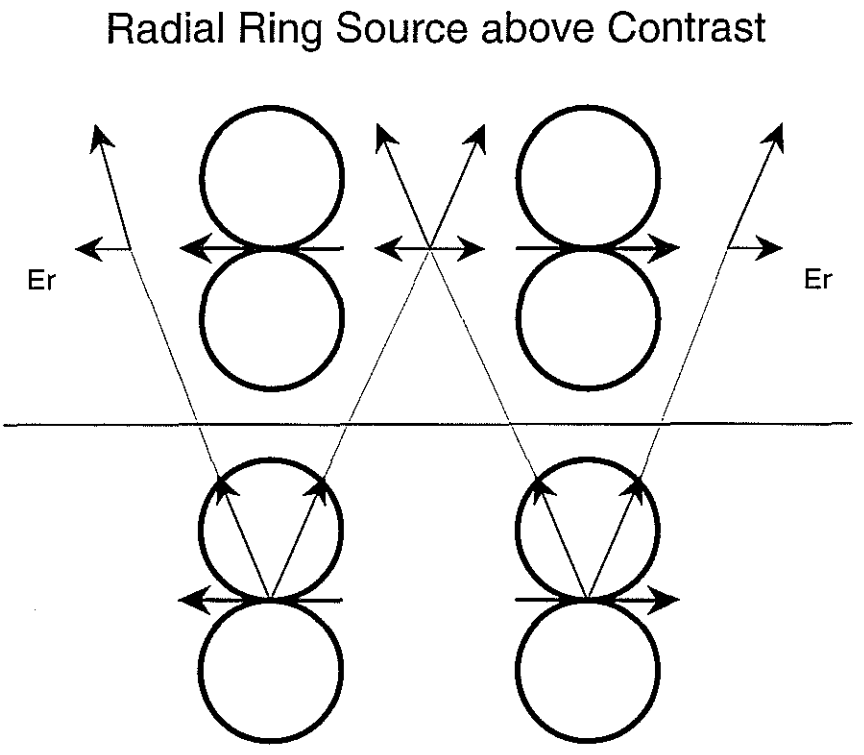

Figure 5: Radial ring source above a contrast.

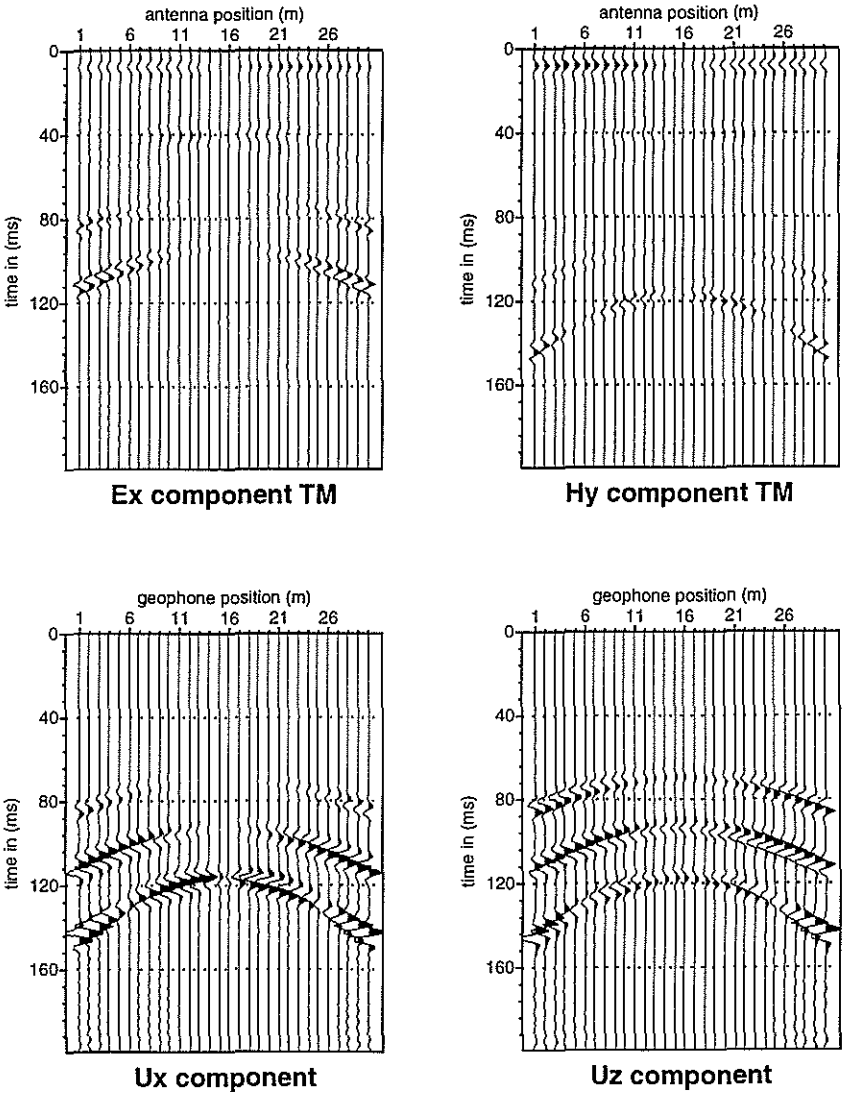

Figure 6: The mechanical displacement component seismograms and the TM mode component electroseismograms, without direct waves, calculated for a radial ring source above a one interface model.

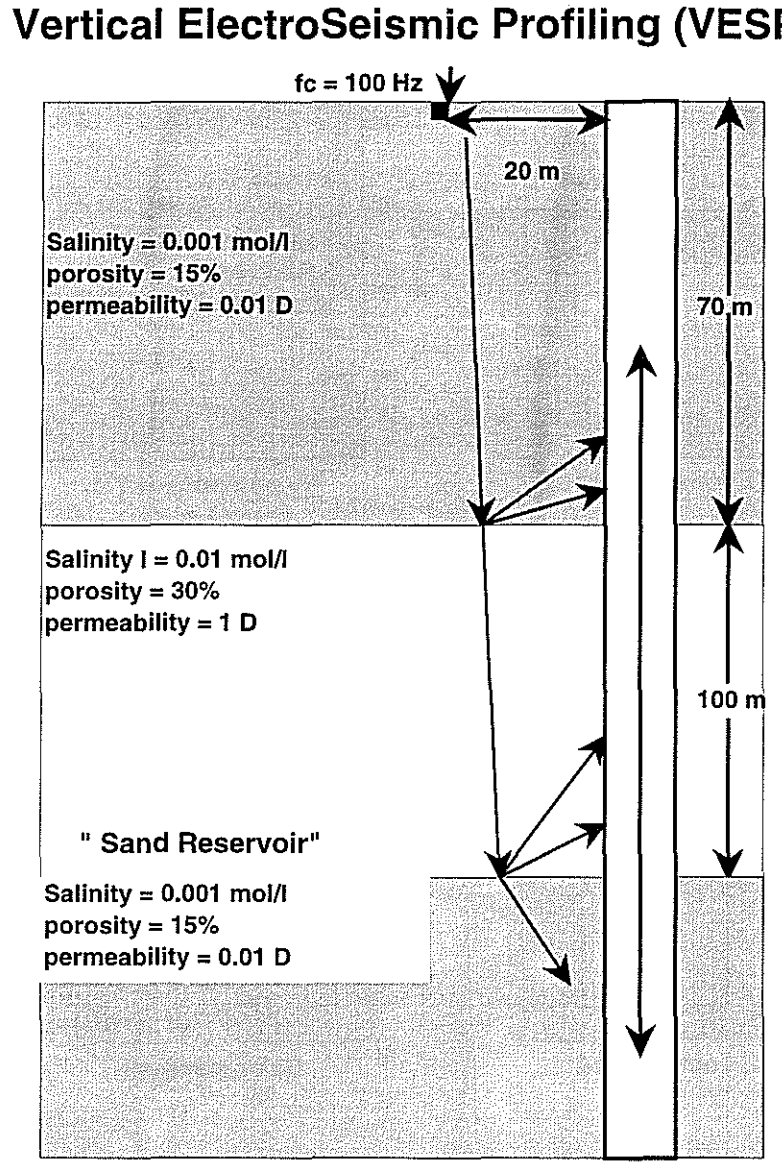

Figure 7: An explosive and vertical point source in a Vertical Electroseismic Profiling geometry (reservoir sand saturated with one fluid type).

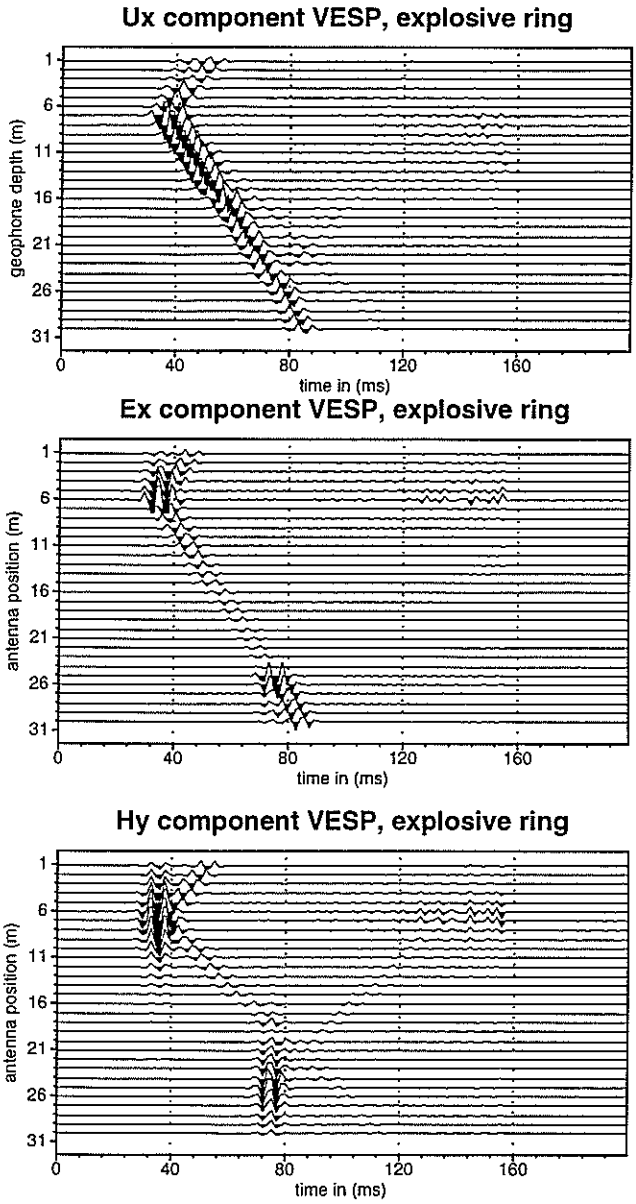

Figure 8: The mechanical displacement component seismogram and the TM mode component electroseismograms calculated for an explosive ring source without direct waves in a Vertical Electroseismic Profiling geometry.

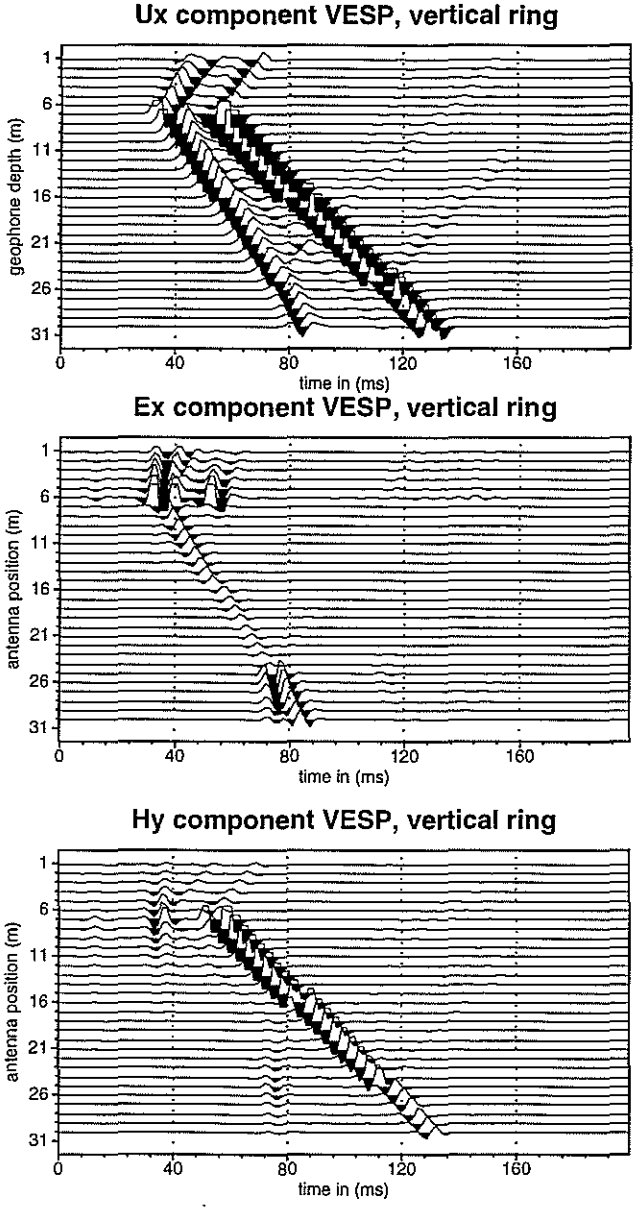

Figure 9: The mechanical displacement component seismogram and the TM mode component electroseismograms calculated for a vertical ring source without direct waves in a Vertical Electroseismic Profiling geometry.

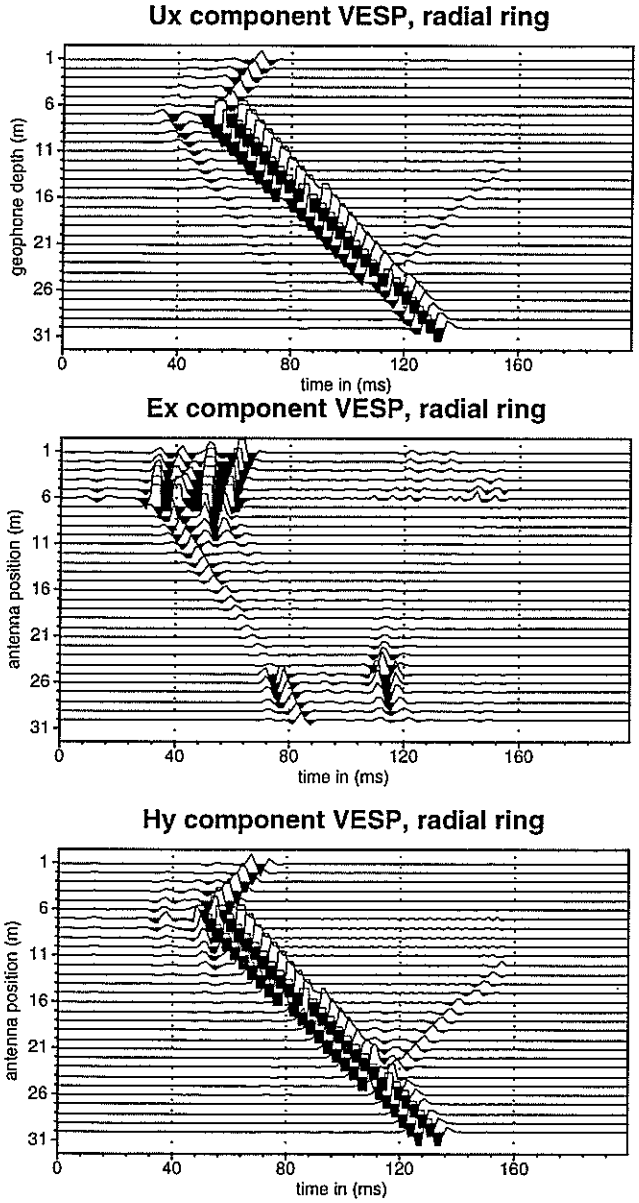

Figure 10: The mechanical displacement component seismogram and the TM mode component electroseismograms calculated for a radial ring source without direct waves in a Vertical Electroseismic Profiling geometry.

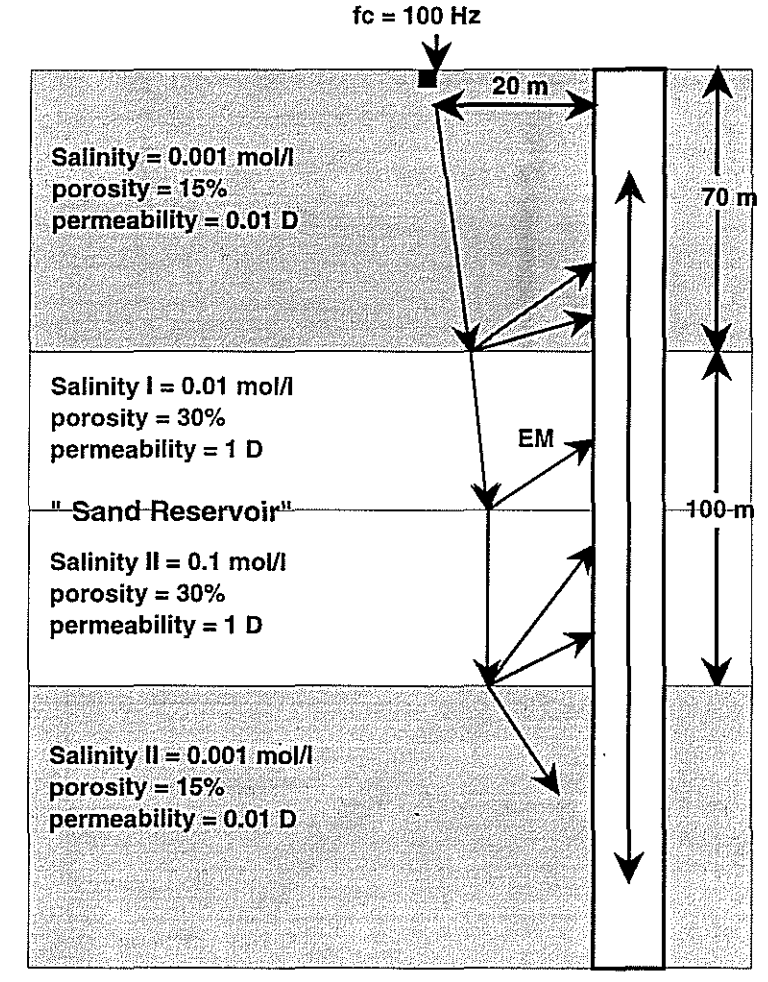

Figure 11: An explosive and vertical point source in a Vertical Electroseismic Profiling geometry (reservoir sand saturated with two fluid types).

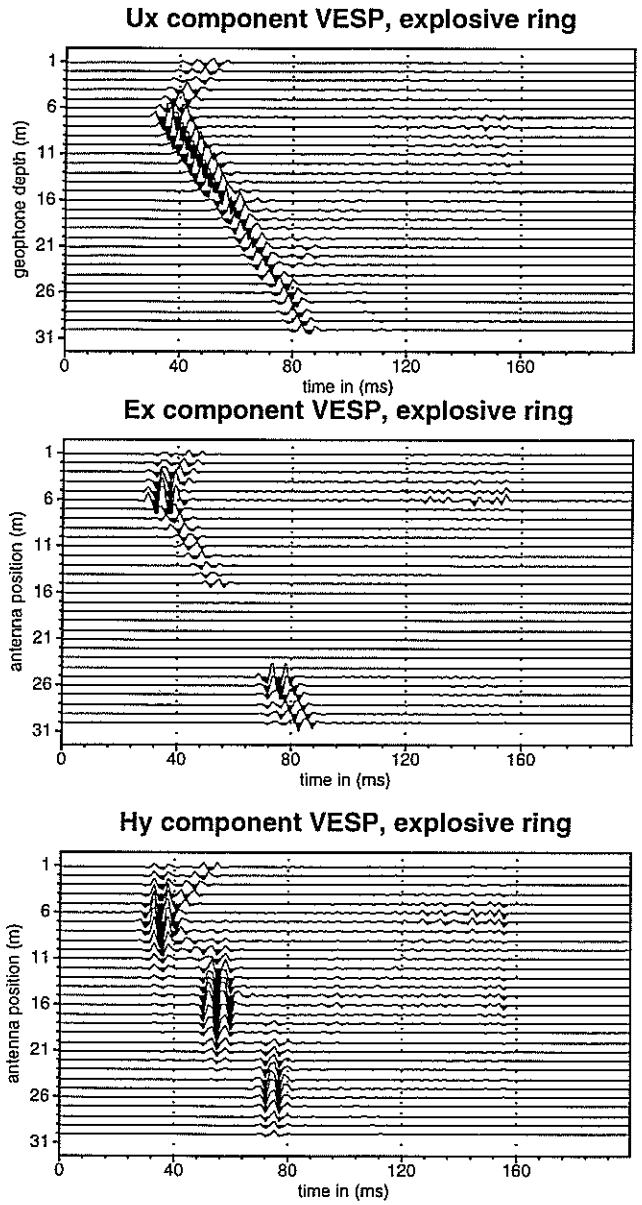

Figure 12: The mechanical displàcement component seismogram and the TM mode component electroseismograms calculated for an explosive ring source without direct waves in a Vertical Electroseismic Profiling geometry with an additional electrical contrast.

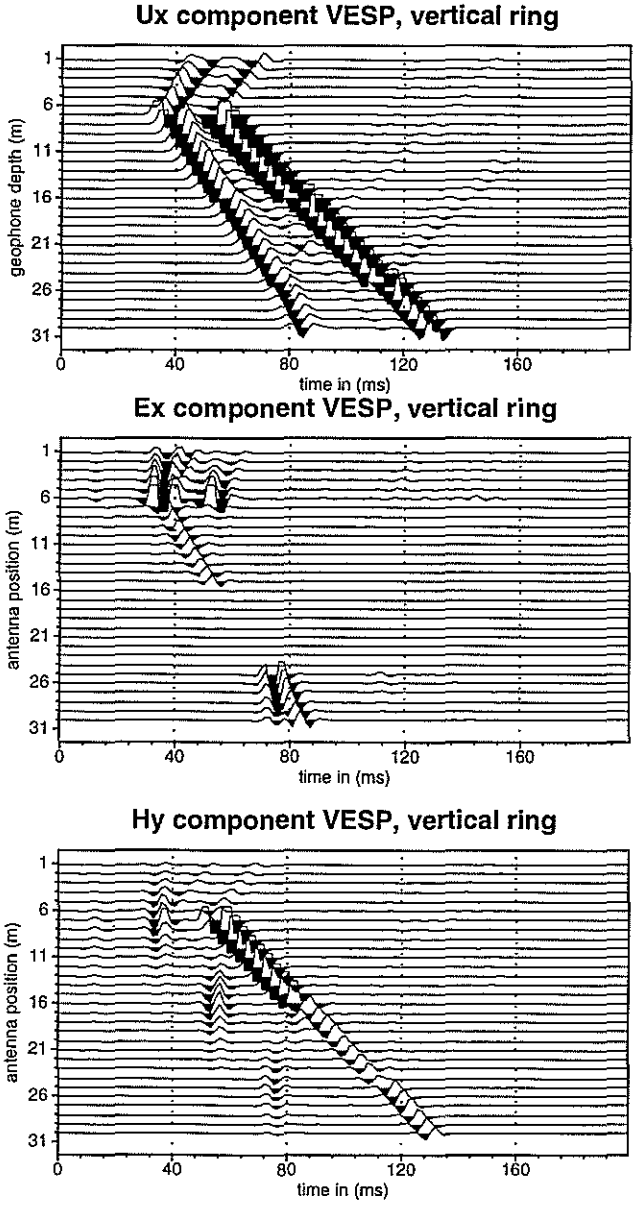

Figure 13: The mechanical displacement component seismogram and the TM mode component electroseismograms calculated for a vertical ring source without direct waves in a Vertical Electroseismic Profiling geometry with an additional electrical contrast.

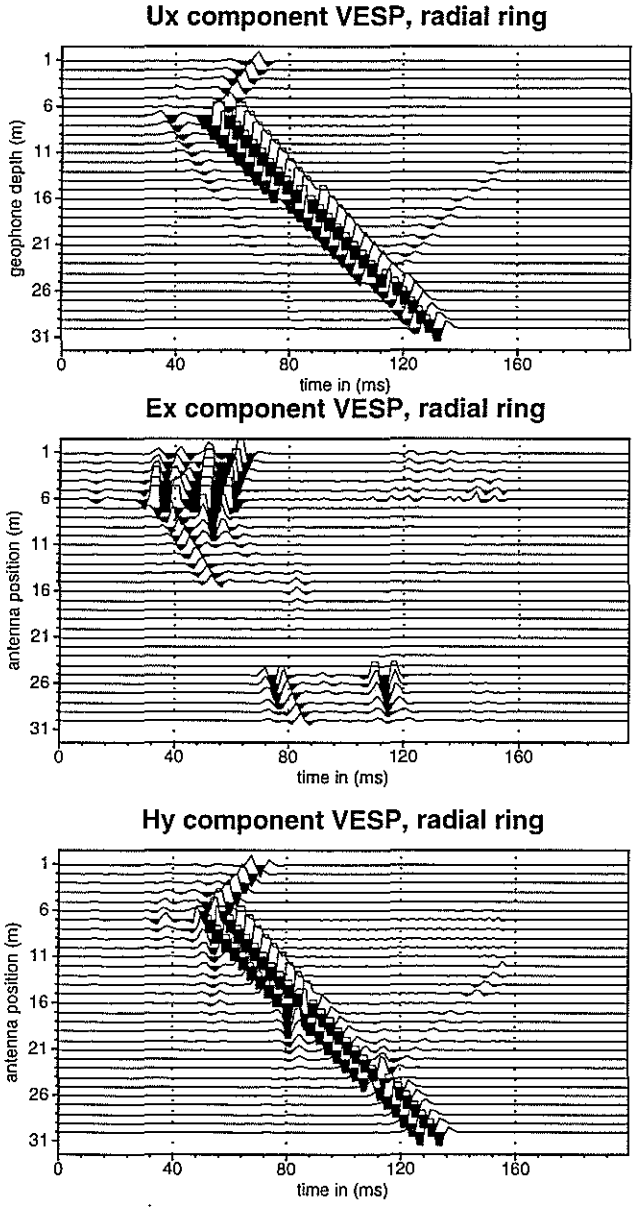

Figure 14: The mechanical displacement component seismogram and the TM mode component electroseismograms calculated for a radial ring source without direct waves in a Vertical Electroseismic Profiling geometry with an additional electrical contrast.